ARMY RESEARCH LABORATORY

An Atomistic-to-Continuum Framework for Nonlinear Crystal Mechanics Based on Asymptotic Homogenization

by John D. Clayton and Peter W. Chung

ARL-RP-161 **February 2007**

A reprint from the *Journal of the Mechanics and Physics of Solids,* vol. 54, pp. 1604–1639, 2006.

Approved for public release; distribution is unlimited.

NOTICES

Disclaimers

The findings in this report are not to be construed as an official Department of the Army position unless so designated by other authorized documents.

Citation of manufacturer's or trade names does not constitute an official endorsement or approval of the use thereof.

Destroy this report when it is no longer needed. Do not return it to the originator.

Army Research Laboratory
Aberdeen Proving Ground, MD 21005-5066

ARL-RP-161 **February 2007**

An Atomistic-to-Continuum Framework for Nonlinear Crystal Mechanics Based on Asymptotic Homogenization

John D. Clayton
Weapons and Materials Research Directorate, ARL

Peter W. Chung
Computational and Information Sciences Directorate, ARL

A reprint from the *Journal of the Mechanics and Physics of Solids*, vol. 54, pp. 1604–1639, 2006.

Approved for public release; distribution is unlimited.

REPORT DOCUMENTATION PAGE

Form Approved
OMB No. 0704-0188

Public reporting burden for this collection of information is estimated to average 1 hour per response, including the time for reviewing instructions, searching existing data sources, gathering and maintaining the data needed, and completing and reviewing the collection information. Send comments regarding this burden estimate or any other aspect of this collection of information, including suggestions for reducing the burden, to Department of Defense, Washington Headquarters Services, Directorate for Information Operations and Reports (0704-0188), 1215 Jefferson Davis Highway, Suite 1204, Arlington, VA 22202-4302. Respondents should be aware that notwithstanding any other provision of law, no person shall be subject to any penalty for failing to comply with a collection of information if it does not display a currently valid OMB control number.

PLEASE DO NOT RETURN YOUR FORM TO THE ABOVE ADDRESS.

1. REPORT DATE *(DD-MM-YYYY)* February 2007	**2. REPORT TYPE** Reprint	**3. DATES COVERED (From - To)** October 2004–October 2006

4. TITLE AND SUBTITLE
An Atomistic-to-Continuum Framework for Nonlinear Crystal Mechanics Based on Asymptotic Homogenization

5a. CONTRACT NUMBER

5b. GRANT NUMBER

5c. PROGRAM ELEMENT NUMBER

6. AUTHOR(S)
John D. Clayton and Peter W. Chung

5d. PROJECT NUMBER
DRI-FY05-CIS-10

5e. TASK NUMBER

5f. WORK UNIT NUMBER

7. PERFORMING ORGANIZATION NAME(S) AND ADDRESS(ES)
U.S. Army Research Laboratory
ATTN: AMSRD-ARL-WM-TD
Aberdeen Proving Ground, MD 21005-5066

8. PERFORMING ORGANIZATION REPORT NUMBER
ARL-RP-161

9. SPONSORING/MONITORING AGENCY NAME(S) AND ADDRESS(ES)

10. SPONSOR/MONITOR'S ACRONYM(S)

11. SPONSOR/MONITOR'S REPORT NUMBER(S)

12. DISTRIBUTION/AVAILABILITY STATEMENT
Approved for public release; distribution is unlimited.

13. SUPPLEMENTARY NOTES
A reprint from the *Journal of the Mechanics and Physics of Solids*, vol. 54, pp. 1604–1639, 2006.

14. ABSTRACT

Presented is a multiscale methodology enabling description of the fundamental mechanical behavior of crystalline materials at the length scale of a macroscopic continuum (i.e., millimeter resolution) given a characterization of discrete atomic interactions at the nanoscale (i.e., angstrom resolution). Asymptotic homogenization methods permit the calculation of effective mechanical properties (e.g. strain energy, stress, and stiffness) of a representative crystalline volume element containing statistically periodic defect structures. From a numerical standpoint, the theoretical–computational method postulated and implemented here in the context of lattice statics enables prediction of minimum energy configurations of imperfect atomic-scale crystals deformed to finite strain levels. Numerical simulations demonstrate the utility of our framework for the particular case of body-centered-cubic tungsten. Elastic stiffness and energetic properties of periodic unit cells containing vacancies, screw dislocations, and low-angle twist boundaries are computed. Nonlinear aspects of elastic behavior in the context of plastic flow are then modeled from the perspective of atomistic-to-continuum homogenization, following the introduction of a minimal set of kinetic assumptions required to account for the propagation of dislocations across the unit cell at finite deformations.

15. SUBJECT TERMS
multiscale, homogenization, molecular dynamics, dislocations, vacancies

16. SECURITY CLASSIFICATION OF:			**17. LIMITATION OF ABSTRACT**	**18. NUMBER OF PAGES**	**19a. NAME OF RESPONSIBLE PERSON**
a. REPORT	**b. ABSTRACT**	**c. THIS PAGE**			John D. Clayton
UNCLASSIFIED	UNCLASSIFIED	UNCLASSIFIED	UL	42	**19b. TELEPHONE NUMBER** (*Include area code*) 410-306-0975

Available online at www.sciencedirect.com
SCIENCE @ DIRECT®
Journal of the Mechanics and Physics of Solids
54 (2006) 1604–1639
JOURNAL OF THE MECHANICS AND PHYSICS OF SOLIDS
www.elsevier.com/locate/jmps

An atomistic-to-continuum framework for nonlinear crystal mechanics based on asymptotic homogenization

John D. Clayton*, Peter W. Chung

U.S. Army Research Laboratory, Aberdeen Proving Ground, MD 21005, USA

Received 1 November 2005; received in revised form 21 February 2006; accepted 28 February 2006

Abstract

Presented is a multiscale methodology enabling description of the fundamental mechanical behavior of crystalline materials at the length scale of a macroscopic continuum (i.e., millimeter resolution) given a characterization of discrete atomic interactions at the nanoscale (i.e., angstrom resolution). Asymptotic homogenization methods permit the calculation of effective mechanical properties (e.g. strain energy, stress, and stiffness) of a representative crystalline volume element containing statistically periodic defect structures. From a numerical standpoint, the theoretical–computational method postulated and implemented here in the context of lattice statics enables prediction of minimum energy configurations of imperfect atomic-scale crystals deformed to finite strain levels. Numerical simulations demonstrate the utility of our framework for the particular case of body-centered-cubic tungsten. Elastic stiffness and energetic properties of periodic unit cells containing vacancies, screw dislocations, and low-angle twist boundaries are computed. Nonlinear aspects of elastic behavior in the context of plastic flow are then modeled from the perspective of atomistic-to-continuum homogenization, following the introduction of a minimal set of kinetic assumptions required to account for the propagation of dislocations across the unit cell at finite deformations.

Published by Elsevier Ltd.

Keywords: Multiscale; Homogenization; Molecular dynamics; Dislocations; Vacancies

---

*Corresponding author. Tel.: +1 410 306 0975; fax: +1 410 306 0783.
E-mail address: jclayton@arl.army.mil (J.D. Clayton).

0022-5096/$ - see front matter Published by Elsevier Ltd.
doi:10.1016/j.jmps.2006.02.004

1. Introduction

Atomistic-to-continuum scale transitioning techniques have come to the fore in recent years, accompanying and supporting widespread interest in engineering of nanoscopic structures (Rudd and Broughton, 2000; Ghoniem et al., 2003; Fish and Chen, 2004). Although marked increases in computing power over the last two decades have facilitated large-scale atomistic calculations (cf. Seppälä et al., 2004), spatial and temporal scale-transitioning schemes are presently in high demand since, at the current rate of increase in computational performance, many years still remain before computers will attain the capability to simulate the mechanical response (and/or thermal, electrical, or magnetic response) of enough atoms, over a time scale of relevant duration, to realistically address design of components or microstructures possessing spatial dimensions on the order of micrometers or larger.

Existing atomistic-to-continuum modeling methods may be loosely grouped into two categories: simultaneous or coupled approaches and sequential or decoupled approaches. Simultaneous methods involve concurrent solution of governing equations at multiple length scales (e.g. quantum mechanics, molecular dynamics, continuum mechanics), with different regions of the spatial domain addressed by governing equations corresponding to the associated scale of resolution of that region. Various algorithms, often quite formidable with regards to numerical implementation, are then used to bridge or "handshake" neighboring regions of differing resolution, for example regions considering molecular dynamics and continuum mechanics. Recent examples of coupled simultaneous methods include, for example, the quasi-continuum theory (Tadmor et al., 1996; Shenoy et al., 1999), the three-scale bridging technique of Broughton et al. (1999), and the dynamic bridging scale method of Park et al. (2005). Such methods are efficient for solving problems wherein the bulk of the material remains relatively homogeneous (and amenable to a coarse-scale solution), with the fine scale physics confined to a small volume of interest, such as at a crack tip, indentation region, or grain or phase boundary.

In contrast, sequential decoupled methods do not involve direct matching of boundary conditions at multiple scales of resolution. Instead, fine scale calculations are conducted, and then the pertinent information from the fine scale solutions is transferred to enhance the representation of the response modeled at the coarse scale. For example, atomistic-scale simulations of the motion of a representative number of atoms may be used to extract bulk elastic and/or plastic properties (Hao et al., 2004) or interfacial properties (Spearot et al., 2005) for subsequent implementation in continuum mechanics-based models. Methods of this nature include approaches based on simultaneous conservation of mass, momentum, and energy at disparate resolutions (Zhou and McDowell, 2002) as well as those predicated on decomposition of the displacement vector into local and global components (Hughes et al., 1998; Hao et al., 2004).

The asymptotic homogenization technique forwarded in the present paper (see also Chung and Namburu, 2003; Chung, 2004) falls into the (latter) category of spatially decoupled methods. In this approach, discrete calculations are conducted at the atomistic level, with each characteristic volume element (i.e., unit cell) of atoms subjected to periodic boundary conditions. Asymptotic homogenization methods (Bensoussan et al., 1978; Sanchez-Palencia, 1980) are concurrently employed to deduce the macroscopic tangent stiffness associated with the mechanical response of the aggregate. The Cauchy–Born approximation (cf. Ericksen, 1984) is invoked for imposition of the bulk continuum deformation, with the fine scale deformation of the atoms identified with the inner displacements in the asymptotic approximation. In this way, the fine scale deformation (of the atoms) near defect cores is corrected with the inner displacements from the homogenization solution, thereby resulting in a lower-energy state for the system than would be achieved via imposition of a uniform deformation gradient over all atoms comprising the unit cell. The present approach is ideal for addressing the response of microstructures containing spatially periodically distributed defects because only one or a few defects need be simulated explicitly at the atomistic level within the context of the periodicity assumption invoked in our homogenization scheme. However, due to this very same periodicity assumption, the method suffers in the sense that isolated (i.e., nonrepeating) defects cannot be easily modeled. Our scaling concept is sketched in Fig. 1.

The atomistic-continuum homogenization technique forwarded here is characterized by several distinctive features in comparison to alternative multiscale formulations. First, asymptotic homogenization methods embody weak convergence in the two-scale continuum sense (Nguetseng, 1989; Allaire, 1992), following from the transmission of displacement gradients as opposed to displacements across length scales. Secondly, this displacement-free embedding also obviates the need in our approach for potentially overly restrictive boundary conditions between atomistic and continuum domains. Lastly, in contrast to sequential modeling schemes in which material information is evaluated at a finer scale and then passed to a coarser one, the asymptotic homogenization method employs a self-consistent set of governing equations simultaneously involving the fine- and coarse-scale descriptions.

Previous research (Chung and Namburu, 2003; Chung, 2004) addressed the effects of pre-existing point defects on the effective elastic stiffness and strain energy density of graphene. One focus of the present effort centers on the mechanical properties induced by dislocations, the primary carriers of plastic deformation in crystalline metals. Owing to the notion that the flux of dislocations leaves the crystal lattice relatively unperturbed upon complete glide across the periodic unit cell, we appeal to the notion of an evolving relaxed intermediate or natural configuration (Eckart, 1948; Bilby et al., 1957; Teodosiu, 1969; Asaro, 1983). In this approach, finite inelastic (i.e., plastic) deformation is accounted for by

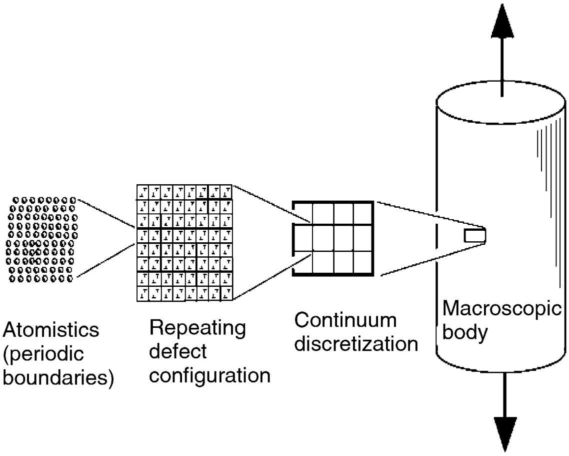
Atomistics (periodic boundaries)
Repeating defect configuration
Continuum discretization
Macroscopic body

Fig. 1. Multiscale modeling schematic.

the evolution of this relaxed configuration, as dictated by the dislocation flux through the volume element. The instantaneous thermoelastic response of the element is measured with respect to the natural configuration, and driving forces for defect propagation are calculated at the current state or time instant, in order to project the intermediate configuration forward temporally. Along similar lines, in an effort to connect nonlinear continuum elasticity theory with the results of discrete atomistic calculations, Lill and Broughton (2000) invoked the idea of an 'obviated reference lattice' characterized by a slowly varying time dependence of the relaxed intermediate state, with a strain threshold introduced above which relaxation from the elastically loaded state takes place. Groma and Pawley (1993) investigated an analogous problem via discrete dislocation dynamics simulations (as opposed to atomistics), considering in their case the superposition of elastic stress fields from the defect ensemble as well as the energetically driven generation of new defects.

Mechanical properties of interest in the present context include the elastic stiffness and energy of crystalline materials in the presence of defects contained within the volume element. We find that our decoupled approach of simultaneously modeling two length scales readily enables parametric variations of the defect density via the prescription of the number of atoms in the fine scale representation relative to the total number of defects embedded within the periodic unit cell. Our framework is implemented numerically and applied first to study the nonlinear elastic response of body-centered cubic (BCC) tungsten (W) containing periodically distributed vacancies, screw dislocations, screw dislocation dipoles, and low-angle twist boundaries (also described here using the disclination concept of Li (1972)). In the above simulations, unit cells are deformed in uniaxial stretch to 2.5% elongation. Our computational method is demonstrated, via direct comparison with conjugate gradient-based lattice statics, to be an efficient means of predicting minimum energy configurations of imperfect atomic-scale lattices subjected to finite deformations. Next, results of larger-deformation shear simulations (to 10% applied shear strain) are reported for the case of screw dislocation glide in BCC W, in which the evolving intermediate configuration is updated assuming monotonic single slip occurs as resolved shear stresses exceed the Peierls threshold (cf. Hirth and Lothe, 1982). The computational procedure involves determination of a correction to the macroscopically imposed deformation of the atoms in the vicinity of defects. Additional details regarding numerical implementation, efficiency, and validation can be found in a companion paper (Chung and Clayton, 2006).

The remainder of this paper is organized as follows. Section 2 features derivations of the multiscale homogenization equations applicable to nonlinear elastic problems. Section 3 introduces the concept of an evolving reference configuration to address finite deformation plasticity and the corresponding inelastic deformation gradient, as well as transformation rules for the multiscale equations in the presence of this evolving frame. Additional assumptions and limitations of our method relating atomistic variables, defect kinetics, and continuum fields are given in Section 4, followed by a description of the numerical implementation in Section 5. We present results of demonstrative simulations in Section 6 and offer perspective on the utility of our theory and results in Section 7. Vectors and tensors are written in boldface type, with scalars and individual components of vectors and tensors written in italic font. The indicial notation is frequently employed for clarity of presentation, with summation implied over repeated indices, e.g. $A^iB_i = A^1B_1 + A^2B_2 + A^3B_3$ when $i = 1, 2, 3$.

2. Two-scale asymptotic homogenization

2.1. Governing equations

Reference and current configurations of a continuous body are introduced, denoted by B_0 and B, respectively. Let $\mathbf{X}$ and $\mathbf{x}$ represent coordinates spanning the reference and spatial frames, and let $x^a = x^a(X^A, t)$, with t denoting time. The deformation gradient or tangent mapping $\mathbf{F}$ from B_0 to B is then written

$$\mathbf{F} = \frac{\partial \mathbf{x}}{\partial \mathbf{X}}, \quad F^a_{.A} = \frac{\partial x^a}{\partial X^A}. \tag{1}$$

The following strain measures are also introduced, where $G_{AB} = \partial_A \mathbf{X} \bullet \partial_B \mathbf{X}$ and $g_{ab} = \partial_a \mathbf{x} \bullet \partial_b \mathbf{x}$ denote, respectively, metric tensors in reference and spatial coordinate systems:

$$C_{AB} = F^a_{.A} g_{ab} F^b_{.B}, \quad 2E_{AB} = F^a_{.A} g_{ab} F^b_{.B} - G_{AB}. \tag{2}$$

Let $\boldsymbol{\Sigma}$, $\mathbf{P}$, and $\mathbf{S}$ denote the Cauchy stress, first Piola–Kirchhoff stress, and second Piola–Kirchhoff stress, respectively, related by

$$\Sigma^{ab} = J^{-1} F^a_{.A} P^{bA} = J^{-1} F^a_{.A} S^{AB} F^b_{.B}. \tag{3}$$

Localized forms of the balances of linear and angular momentum are written as follows in the reference frame, assuming quasi-static conditions:

$$P^{aA}_{|A} + B^a = 0, \quad F^a_{.A} P^{bA} = P^{aA} F^b_{.A}, \tag{4}$$

where the vertical bar denotes covariant differentiation and $\mathbf{B}$ is the body force vector per unit reference volume. From Eq. (3) and the second of Eq. (4), we have $\Sigma^{ab} = \Sigma^{(ab)}$ and $S^{AB} = S^{(AB)}$, where parentheses indicate symmetrization, i.e., $2A^{(ab)} = A^{ab} + A^{ba}$ for arbitrary second-rank tensor $\mathbf{A}$. As will be discussed later, neglect of inertia in Eq. (4) restricts our present approach to time-independent applications at the fine scale (i.e., static problems). Multiplying the first of Eq. (4) by virtual displacement $\delta \mathbf{u}$ and integrating over reference volume V, we arrive at the following virtual work principle (cf. Marsden and Hughes, 1983):

$$\int_V P^{aB} g_{ab} (\delta u)^b_{|B} \, \mathrm{d}V = \int_{\partial V} T^a g_{ab} \delta u^b \, \mathrm{d}A + \int_V B^a g_{ab} \delta u^b \, \mathrm{d}V, \tag{5}$$

with the traction per unit reference area A given by $T^a = P^{aB} N_B$, where N_B are covariant components of the unit normal vector to external boundary ∂V. Let us assume the existence of a free-energy potential Ψ per unit reference volume on B_0, with the stress tensor satisfying the following hyperelastic relationships:

$$S^{AB} = 2 \frac{\partial \Psi}{\partial C_{AB}} = \frac{\partial \Psi}{\partial E_{AB}}. \tag{6}$$

For the particular case of first-order hyperelasticity, Eq. (6) becomes

$$S^{AB} = \frac{\partial^2 \Psi}{\partial E_{AB} \partial E_{CD}} E_{CD} = \mathbb{C}^{ABCD} E_{CD}, \tag{7}$$

where $\mathbb{C}^{ABCD} = \mathbb{C}^{(AB)(CD)}$ is the fourth-rank elastic modulus tensor in the reference frame. Substituting Eq. (6) into Eq. (5) and appealing to Eq. (3), we then have

$$\int_V 2F^a_{.A}\frac{\partial \Psi}{\partial C_{AB}} g_{ab}(\delta u)^b_{|B}\,\mathrm{d}V = \int_{\partial V} T^a g_{ab}\delta u^b\,\mathrm{d}A + \int_V B^a g_{ab}\delta u^b\,\mathrm{d}V. \tag{8}$$

2.2. *Asymptotic homogenization*

Our link between atomistic and continuum resolutions is achieved via the asymptotic homogenization technique (Chung and Namburu, 2003; Chung, 2004). Let fine and coarse length scales (i.e., the microscale and macroscale) be spanned by coordinates $y^a = y^a(Y^A, t)$ and $x^a = x^a(X^A, t)$, respectively. Notice that in the present scheme, both scales are parameterized by the same temporal variable t. Multiscale coordinates are related by

$$x^a = \varepsilon y^a, \quad X^A = \varepsilon Y^A, \tag{9}$$

where ε is a small scalar assumed constant throughout the time history of deformation. We introduce coarse- and fine scale displacements $\mathbf{u}$ and $\mathbf{v}$, respectively, restricted below to coincident Cartesian coordinate systems in the reference and spatial frames:

$$u^a = x^a - \delta^a_A X^A, \quad v^a = y^a - \delta^a_{.A} Y^A, \tag{10}$$

with the Cartesian shifter $\delta^a_{.A} = 1$ for $a = A$ and $\delta^a_{.A} = 0$ for $a \neq A$. Deformation gradients then follow as

$$F^a_{.A} = \frac{\partial u^a}{\partial X^A} + \delta^a_{.A}, \quad f^a_{.A} = \frac{\partial y^a}{\partial Y^A} + \delta^a_{.A}. \tag{11}$$

Next we assume an additive decomposition of displacements at the coarse scale (Takano et al., 2000),

$$u^a = \overline{u}^a + \tilde{u}^a = \overline{u}^a + \varepsilon \tilde{v}^a, \tag{12}$$

where $\overline{u}^a$ represents the displacement that would exist in a microscopically homogeneous medium and $\tilde{u}^a$ is the perturbation in displacement due to fine scale heterogeneity, with corresponding fine scale representation $\tilde{v}^a$. The corresponding microscopic decomposition is

$$v^a = \varepsilon^{-1} u^a = \overline{v}^a + \tilde{v}^a = \left(F^a_{.A} - \delta^a_{.A}\right) Y^A + \tilde{v}^a, \tag{13}$$

with $\overline{v}^a$ the microscopic displacement arising from the projection to the fine scale of the macroscopic deformation gradient $F^a_{.A}$. Differentiating $\mathbf{u}$ of Eq. (12) with respect to X^A gives

$$\frac{\partial}{\partial X^A}(\overline{u}^a + \varepsilon \tilde{v}^a) = \frac{\partial \overline{u}^a}{\partial X^A} + \frac{\partial \tilde{v}^a}{\partial Y^A}, \tag{14}$$

where we have appealed to the second of Eq. (9). From Eq. (11), we then arrive at the decomposition

$$F^a_{.A} = \frac{\partial \overline{u}^a}{\partial X^A} + \frac{\partial \tilde{v}^a}{\partial Y^A} + \delta^a_{.A} = \left(\frac{\partial \overline{u}^a}{\partial X^A}\delta^A_{.\bar{\alpha}} + \delta^a_{.\bar{\alpha}}\right)\tilde{F}^{\bar{\alpha}}_{.A} = \overline{F}^a_{.\bar{\alpha}}\tilde{F}^{\bar{\alpha}}_{.A}, \tag{15}$$

where $\overline{F}^a_{.\bar{\alpha}}$ is the deformation gradient under microscopically homogeneous conditions and $\tilde{F}^{\bar{\alpha}}_{.A} = \overline{F}^{-1\bar{\alpha}}_{.a} F^a_{.A}$ depends upon the gradient of $\tilde{\mathbf{v}}$ and thus accounts for heterogeneity due to defect fields. Barred Greek indices denote a third configuration $\overline{B}$ for the material associated with the multiplicative decomposition in the last of Eq. (15).

Note that the left-hand side of Eq. (8) can be written as follows in Cartesian coordinates:

$$\int_V 2F^a_{.A}\frac{\partial\Psi}{\partial C_{AB}}g_{ab}(\delta u)^b_{|B}\,\mathrm{d}V=\int_V\frac{\partial\Psi}{\partial F^a_{.B}}\frac{\partial(\delta u^a)}{\partial X^B}\,\mathrm{d}V, \tag{16}$$

and that the total displacement variation δu^a can be expressed, from Eq. (12), as

$$\delta u^a=\delta\overline{u}^a+\varepsilon\delta\tilde{v}^a. \tag{17}$$

Substituting Eqs. (16) and (17) into Eq. (8) gives

$$\begin{aligned}&\int_V\frac{\partial\Psi}{\partial F^a_{.B}}\frac{\partial}{\partial X^B}(\delta\overline{u}^a+\varepsilon\delta\tilde{v}^a)\,\mathrm{d}V\\&\quad=\int_{\partial V}T^a g_{ab}(\delta\overline{u}^b+\varepsilon\delta\tilde{v}^b)\,\mathrm{d}A+\int_V B^a g_{ab}(\delta\overline{u}^b+\varepsilon\delta\tilde{v}^b)\,\mathrm{d}V,\end{aligned} \tag{18}$$

which is then volume-averaged over micro-domain Y to yield

$$\begin{aligned}&\frac{1}{Y}\int_Y\int_V\frac{\partial\Psi}{\partial F^a_{.B}}\left(\frac{\partial(\delta\overline{u}^a)}{\partial X^B}+\frac{\partial(\delta\tilde{v}^a)}{\partial Y^B}\right)\mathrm{d}V\,\mathrm{d}Y\\&\quad=\frac{1}{Y}\int_Y\int_{\partial V}T^a g_{ab}(\delta\overline{u}^b+\varepsilon\delta\tilde{v}^b)\,\mathrm{d}A\,\mathrm{d}Y+\frac{1}{Y}\int_Y\int_V B^a g_{ab}(\delta\overline{u}^b+\varepsilon\delta\tilde{v}^b)\,\mathrm{d}V\,\mathrm{d}Y.\end{aligned} \tag{19}$$

Eq. (19) is satisfied in the asymptotic limit $\varepsilon\to 0$ only if the following conditions hold:

$$\frac{1}{Y}\int_Y\int_V\frac{\partial\Psi}{\partial F^a_{.B}}\frac{\partial(\delta\overline{u}^a)}{\partial X^B}\,\mathrm{d}V\,\mathrm{d}Y=\int_{\partial V}T^a g_{ab}\delta\overline{u}^b\,\mathrm{d}A+\int_V B^a g_{ab}\delta\overline{u}^b\,\mathrm{d}V\quad(\forall\,\delta\overline{u}^a), \tag{20}$$

$$\frac{1}{Y}\int_Y\int_V\frac{\partial\Psi}{\partial F^a_{.B}}\frac{\partial(\delta\tilde{v}^a)}{\partial Y^B}\,\mathrm{d}V\,\mathrm{d}Y=0\quad(\forall\delta\tilde{v}^a). \tag{21}$$

Notice that coarse-scale Eq. (20) and fine scale Eq. (21) are coupled through the constitutive dependency $\Psi=\Psi(\mathbf{F}(\partial\overline{\mathbf{u}}/\partial\mathbf{X},\partial\tilde{\mathbf{v}}/\partial\mathbf{Y}))$.

3. Homogenization under an evolving intermediate frame

3.1. Multiplicative kinematics

Assume now that we are dealing with an elastic–plastic material in the usual continuum sense wherein the deformation gradient $\mathbf{F}$ is decomposed multiplicatively into a lattice part, $\mathbf{F}^{\mathbf{L}}$, and a plastic part, $\mathbf{F}^{\mathbf{P}}$ (Bilby et al., 1957; Teodosiu, 1969):

$$\mathbf{F}=\mathbf{F}^{\mathbf{L}}\mathbf{F}^{\mathbf{P}},\quad F=F^{La}_{\alpha}F^{P\alpha}_{.A}. \tag{22}$$

Implicit in Eq. (22) is the existence of intermediate configuration $\tilde{B}$, with $\mathbf{F}^{\mathbf{P}}$ the tangent mapping between B_0 and $\tilde{B}$, and $\mathbf{F}^{\mathbf{L}}$ the tangent mapping from $\tilde{B}$ to B. The plastic map $\mathbf{F}^{\mathbf{P}}$ reflects contributions to the total deformation that leave the lattice unperturbed, such as the flux of mobile dislocations. The lattice map $\mathbf{F}^{\mathbf{L}}$ includes all other kinematic contributions, including rigid body motion of the lattice, recoverable elastic stretch fields associated with the applied loads on the body, and residual elastic stretch fields attributed to microscopic heterogeneity (e.g., defects contained within the local volume element or periodic unit cell). Thus $\tilde{B}$ is identified with a relaxed natural configuration of finite plasticity theory (Eckart, 1948).

3.2. Governing equations

In an elastic–plastic body, it is typically assumed that the free energy depends only upon that part of the deformation that affects the lattice, in other words,

$$\tilde{\Psi} = J^{P-1}\Psi(\mathbf{F}, \mathbf{F^P}, \boldsymbol{\xi}, \theta) = \tilde{\Psi}(\mathbf{F^L}, \boldsymbol{\xi}, \theta), \tag{23}$$

where $\tilde{\Psi}$ is measured per unit intermediate volume on $\tilde{B}$, J^P is the Jacobian determinant of $\mathbf{F^P}$, and where we have also included the dependence of the free energy on absolute temperature θ. Additionally, $\boldsymbol{\xi}$ is a vector of internal state variables accounting for deviations in stored energy from that of a perfect lattice. From Eqs. (22) and (23) and assuming an instantaneous hyperelastic response, the first Piola–Kirchhoff stress satisfies

$$P_a^{.A} = \frac{\partial \Psi}{\partial F^a_{.A}} = J^{P-1}\frac{\partial \tilde{\Psi}}{\partial F^{La}_{.\alpha}} F^{P-1A}_{.\alpha}. \tag{24}$$

The balance of linear momentum in Eq. (4) can then be re-written as follows:

$$\left(g^{ab} J^{P-1} F^{P-1A}_{.\alpha} \frac{\partial \tilde{\Psi}}{\partial F^{Lb}_{.\alpha}} \right)_{|A} + B^a = 0. \tag{25}$$

Let us denote the intermediate second Piola–Kirchhoff stress by

$$\tilde{S}^{\alpha\beta} = g^{ab}\frac{\partial \tilde{\Psi}}{\partial F^{Lb}_{.\alpha}} F^{L-1\beta}_{.a} = 2\frac{\partial \tilde{\Psi}}{\partial \tilde{C}_{\alpha\beta}} = \frac{\partial \tilde{\Psi}}{\partial \tilde{E}_{\alpha\beta}}, \tag{26}$$

where

$$\tilde{C}_{\alpha\beta} = F^{La}_{.\alpha} g_{ab} F^{Lb}_{.\beta}, \quad 2\tilde{E}_{\alpha\beta} = \tilde{C}_{\alpha\beta} - \tilde{g}_{\alpha\beta}, \tag{27}$$

with $\tilde{\mathbf{g}}$ the metric tensor on configuration $\tilde{B}$. Note that in Eq. (26), we have made the usual assumption that the dependency of $\tilde{\Psi}$ upon $\mathbf{F^L}$ can be replaced with a dependency upon $\tilde{\mathbf{C}}$ or $\tilde{\mathbf{E}}$, in order to satisfy standard frame indifference arguments (cf. Marsden and Hughes, 1983). Analogous to Eq. (7), for the particular case of first-order hyperelasticity, Eq. (26) becomes

$$\tilde{S}^{\alpha\beta} = \frac{\partial^2 \tilde{\Psi}}{\partial \tilde{E}_{\alpha\beta}\partial \tilde{E}_{\chi\delta}} \tilde{E}_{\chi\delta} = \tilde{\mathbb{C}}^{\alpha\beta\chi\delta}\tilde{E}_{\chi\delta}, \tag{28}$$

with $\tilde{\mathbb{C}}^{\alpha\beta\chi\delta} = \tilde{\mathbb{C}}^{(\alpha\beta)(\chi\delta)}$ the fourth-rank elastic modulus referred to $\tilde{B}$. Eq. (5) can then be written as follows for a hyperelastic–plastic body, upon appealing to Eq. (25)

$$\int_V J^{P-1} F^{P-1A}_{.\alpha} \frac{\partial \tilde{\Psi}}{\partial F^{La}_{.\alpha}} (\delta u)^a_{|A}\, \mathrm{d}V = \int_{\partial V} T^a g_{ab} \delta u^b\, \mathrm{d}A + \int_V B^a g_{ab} \delta u^b\, \mathrm{d}V. \tag{29}$$

3.3. Asymptotic homogenization

Expressions (9)–(15) and (17) apply for the elastic–plastic case. Substituting Eq. (17) into Eq. (29) and using Cartesian coordinates X^A, we have

$$\begin{aligned}\int_V J^{P-1} F^{P-1B}_{.\alpha} \frac{\partial \tilde{\Psi}}{\partial F^{La}_{.\alpha}} \frac{\partial}{\partial X^B} (\delta \bar{u}^a + \varepsilon \delta \tilde{v}^a)\,\mathrm{d}V \\ = \int_{\partial V} T^a g_{ab} (\delta \bar{u}^b + \varepsilon \delta \tilde{v}^b)\,\mathrm{d}A + \int_V B^a g_{ab} (\delta \bar{u}^b + \varepsilon \delta \tilde{v}^b)\,\mathrm{d}V, \end{aligned} \tag{30}$$

leading to the following coupled multiscale equations in the limit as $\varepsilon \to 0$:

$$\frac{1}{Y} \int_Y \int_V J^{P-1} F^{P-1B}_{.\alpha} \frac{\partial \tilde{\Psi}}{\partial F^{La}_{.\alpha}} \frac{\partial (\delta \bar{u}^a)}{\partial X^B}\,\mathrm{d}V\,\mathrm{d}Y = \int_{\partial V} T^a g_{ab} \delta \bar{u}^b\,\mathrm{d}A + \int_V B^a g_{ab} \delta \bar{u}^b\,\mathrm{d}V \quad (\forall\, \delta \bar{u}^a), \tag{31}$$

$$\frac{1}{Y} \int_Y \int_V J^{P-1} F^{P-1B}_{.\alpha} \frac{\partial \tilde{\Psi}}{\partial F^{La}_{.\alpha}} \frac{\partial (\delta \tilde{v}^a)}{\partial Y^B}\,\mathrm{d}V\,\mathrm{d}Y = 0 \quad (\forall \delta \tilde{v}^a). \tag{32}$$

Notice that generally, $\mathbf{F^L}$ and $\mathbf{F^P}$ of Eq. (22) and $\bar{\mathbf{F}}$ and $\tilde{\mathbf{F}}$ of Eq. (15) are four distinct deformation mappings, with corresponding configurations of the body depicted in Fig. 2(a). The former two denote lattice and plastic deformations; the latter two represent micro-homogeneous and micro-heterogeneous deformations, respectively. Under certain circumstances, however, some of these may reduce to the identity map. Possible scenarios are summarized below:

$$\begin{aligned} &\text{Elastoplasticity with defects}: \ \mathbf{F} = \mathbf{F^L F^P} = \bar{\mathbf{F}}\tilde{\mathbf{F}}, \\ &\text{Homogeneous elastoplasticity}: \ \mathbf{F} = \mathbf{F^L F^P} = \bar{\mathbf{F}}, \\ &\text{Elasticity with defects}: \ \mathbf{F} = \mathbf{F^L} = \bar{\mathbf{F}}\tilde{\mathbf{F}}, \\ &\text{Homogeneous elasticity}: \ \mathbf{F} = \mathbf{F^L} = \bar{\mathbf{F}}. \end{aligned} \tag{33}$$

In Eq. (33), "elastoplasticity with defects" is the most general case, for example a crystalline volume element that has sustained dislocation flux during its deformation history and also contains dislocations, possibly immobile. By "homogeneous elastoplasticity" we mean a situation in which dislocations may have traversed the volume element,

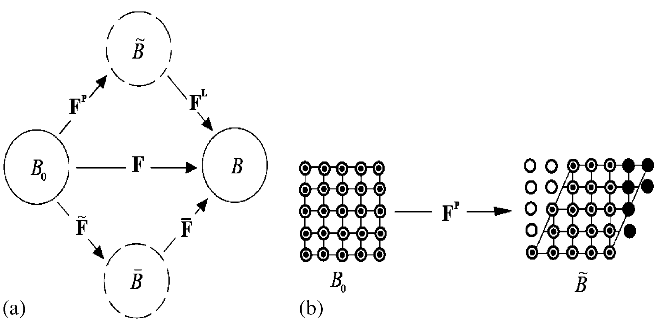

Fig. 2. Deformation mappings and configurations (a), and purely plastic deformation (b).

but no defects or commensurate residual stress fields are contained within. By “elasticity with defects”, we refer to the case in which no defects have traversed the element (i.e., null dislocation flux over the deformation history), but when defects are contained within, leading to microscopic heterogeneity and internal stress fields. This was the situation studied by Chung and Namburu (2003) and Chung (2004), where the representation of point defects was the primary concern. “Homogeneous elasticity” refers to a lattice free of defects over the entire time history of deformation.

4. Multiscale formulation

Here we present kinematic, thermodynamic, and kinetic assumptions needed to relate atomistic and continuum fields and incrementally update intermediate configurations $\tilde{B}$ and $\overline{B}$.

4.1. Discrete and continuum descriptions of lattice quantities

Assume that in reference configuration B_0, the representative volume (i.e., unit cell) for homogenization consists of atoms arranged in a lattice, perhaps imperfect due to the presence of defects. Furthermore, assume that in configuration $\tilde{B}$, the same mass and number of atoms exist in this representative volume, for example upon propagation of dislocations across the unit cell. Individual atomic positions in B_0 and $\tilde{B}$ may not coincide, even though the lattice may look the same to an external observer in each of these two configurations. The position vector for an arbitrary atom m in evolving configuration $\tilde{B}$ is denoted by $\tilde{\mathbf{Z}}_{\langle m\rangle}$, where angled brackets are reserved for atomic labels, which range from 1 to $\mathbb{N}$. Spatial positions $z^a_{\langle j\rangle}$ of atoms in configuration B are then found as follows, in Cartesian coordinates:

$$z^a_{\langle j\rangle} = \delta^a_\alpha \tilde{Z}^\alpha_{\langle j\rangle} + q^a_{\langle j\rangle}, \tag{34}$$

with $\mathbf{q}_{<j>}$ a displacement vector between intermediate and current states for atom m. Let $\tilde{\mathbf{R}}_{\langle j\backslash k\rangle}$ and $\mathbf{r}_{\langle j\backslash k\rangle}$ denote vectors separating atoms a and b in respective configurations $\tilde{B}$ and B, i.e.,

$$\tilde{\mathbf{R}}_{\langle j\backslash k\rangle} = \tilde{\mathbf{Z}}_{\langle k\rangle} - \tilde{\mathbf{Z}}_{\langle j\rangle}, \tag{35}$$

$$\mathbf{r}_{\langle j\backslash k\rangle} = \mathbf{z}_{\langle k\rangle} - \mathbf{z}_{\langle j\rangle}. \tag{36}$$

Making contact with the homogenization theory of Sections 2 and 3, we next assume

$$z^a_{\langle j\rangle} = \overline{F}^{La}_{\langle jk\rangle\alpha} \tilde{Z}^\alpha_{\langle k\rangle} + \tilde{v}^a_{\langle j\rangle}, \tag{37}$$

with summation implied over repeated atomic indices. The first term in Eq. (37), $\overline{F}^{La}_{\langle jk\rangle\alpha} \tilde{Z}^\alpha_{\langle k\rangle}$, accounts for the uniform projection over each periodic cell of the macroscopic lattice deformation field to the fine scale (i.e., the Cauchy–Born approximation), and $\tilde{v}^a_{\langle j\rangle}$ is the discrete atomistic analog of the perturbation in displacement due to microscopic heterogeneity given in previously in Eq. (13), written here for atom m. Notice that $\tilde{v}^a_{\langle j\rangle}$ of Eq. (37) is technically the perturbation in displacement from the intermediate state, whereas $\tilde{v}^a$ of Eq. (13) is a displacement perturbation from the initial reference state. However, if the plastic deformation mapping $\mathbf{F}^\mathbf{P}$ is assumed to leave the lattice properties unaltered, then these displacement perturbations may be considered, for our purposes, to be equivalent. Spatial separation vectors in Eq. (36) then become

$$\mathbf{r}_{\langle j\backslash k\rangle} = \bar{\mathbf{F}}^{\mathbf{L}}\tilde{\mathbf{R}}_{\langle j\backslash k\rangle} + \tilde{\mathbf{v}}_{\langle k\rangle} - \tilde{\mathbf{v}}_{\langle j\rangle} = \bar{\mathbf{F}}^{\mathbf{L}}\tilde{\mathbf{R}}_{\langle j\backslash k\rangle} + \tilde{\mathbf{r}}_{\langle j\backslash k\rangle}, \tag{38}$$

with $\tilde{\mathbf{r}}_{\langle j\backslash k\rangle} = \tilde{\mathbf{v}}_{\langle k\rangle} - \tilde{\mathbf{v}}_{\langle j\rangle}$ accounting for deviations from the Cauchy–Born rule.

Reference state B_0 is related to the intermediate state $\tilde{B}$ as follows. The mapping $\mathbf{F}^{\mathbf{P}}$ represents the cumulative deformation of the material, but not the lattice, due to dislocation glide through the unit cell. For a fixed control volume, once atoms have convected through the lattice due to $\mathbf{F}^{\mathbf{P}}$, B_0 and $\tilde{B}$ appear identical in the fine scale domain if no dislocations are created or destroyed within the volume element, yet net deformation of the material will have taken place at the coarse scale. The same concept is used in classical crystal plasticity theory, e.g. Asaro (1983), wherein the lattice director vectors are assumed to be unaffected by $\mathbf{F}^{\mathbf{P}}$. For a purely plastic process with $\mathbf{F}^{\mathbf{L}} = \mathbf{1}$, new atoms would enter the control volume (i.e., the atomic unit cell) in the identical locations as the old, to replace those that exited due to plastic flow, and the mass of the system would be conserved (the volume would also be conserved for processes in which $J^P = 1$). The concept is illustrated in Fig. 2(b), in which atoms that exit the unit cell are denoted by filled circles, and those that enter the cell by open circles, with the underlying material undergoing pure plastic shear. Though not illustrated explicitly here, immobile dislocations or other stationary defects are admitted within the volume in both configurations, as the influence of such defects on the stored energy and mechanical response is of primary interest in the applications that follow.

Henceforth we assume a free-energy potential depending only upon the relative positions of all atoms (i.e., lattice statics):

$$\tilde{\Psi} = \tilde{\Psi}(\mathbf{q}_{\langle j\rangle}, \tilde{\mathbf{Z}}_{\langle j\rangle}) = \tilde{\Psi}(\mathbf{r}_{\langle 1\backslash 2\rangle}, \mathbf{r}_{\langle 1\backslash 3\rangle}, \mathbf{r}_{\langle 2\backslash 3\rangle}, \ldots \mathbf{r}_{\langle \mathbb{N}-1\backslash \mathbb{N}\rangle}). \tag{39}$$

Analogous to Eq. (39) is the isothermal representation of continuum expression (23):

$$\tilde{\Psi} = \tilde{\Psi}(\mathbf{F}^{\mathbf{L}}, \boldsymbol{\xi}), \tag{40}$$

where $\boldsymbol{\xi}$ accounts for effects on stored energy due to deviations from homogeneous elasticity at the fine scale. Integrating Eq. (32) by parts and applying the divergence theorem over volume Y with oriented surface element $N_A\,\mathrm{d}A$, we arrive at

$$\frac{1}{A}\int_{\partial Y}\int_V J^{P-1}F^{P-1B}_{.a}\frac{\partial\tilde{\Psi}}{\partial F^{La}_{.\alpha}}\delta\tilde{v}^a N_B\,\mathrm{d}V\,\mathrm{d}A = \frac{1}{Y}\int_Y\int_V \frac{\partial}{\partial Y^B}\left(J^{P-1}F^{P-1\;B}_{.\alpha}\frac{\partial\tilde{\Psi}}{\partial F^{La}_{.\alpha}}\right)\delta\tilde{v}^a\,\mathrm{d}V\,\mathrm{d}Y. \tag{41}$$

Localizing the volume integral on the right-hand side of Eq. (41) and considering all admissible variations $\delta\tilde{\mathbf{v}}$, the microscopic linear momentum balance becomes

$$\frac{\partial}{\partial Y^B}\left(J^{P-1}F^{P-1\;B}_{.\alpha}\frac{\partial\tilde{\Psi}}{\partial F^{La}_{.\alpha}}\right) = \frac{\partial P^{.B}_{a}}{\partial Y^B} = 0 \quad (\text{in } Y) \tag{42}$$

as the area integral vanishes since we may choose $\delta\tilde{\mathbf{v}} = \mathbf{0}$ on $A = \partial Y$. Eq. (42) is quite general in the sense that no assumption is made on the order of the incremental elastic response; for example, higher-order elastic constants are admitted in the sense of material nonlinearity. For algorithmic purposes, however, we find it advantageous to assume a quadratic energy dependency along the lines of Eq. (28), an appropriate assumption for most engineering metals undergoing quasi-static deformations. The overall elastic stress–strain response may still be nonlinear in our formulation, however, as we allow the tangent elastic stiffness tensor to vary with elastic deformation $\mathbf{F}^{\mathbf{L}}$, and the formulation may also be considered nonlinear in the geometric sense, as finite deformations are addressed. We thus re-write Eq. (42) as

$$\frac{\partial}{\partial Y^B}\left(J^{P-1}F^{P-1B}_{.\alpha}\frac{\partial^2\tilde{\Psi}}{\partial F^{La}_{.\alpha}\partial F^{Lb}_{.\beta}}(F^{Lb}_{.\beta}-\delta^b_{.\beta})\right)=\frac{\partial}{\partial Y^B}\left(J^{P-1}F^{P-1B}_{.\alpha}\hat{\mathbb{C}}^{\alpha\beta}_{ab}(F^{Lb}_{.\beta}-\delta^b_{.\beta})\right)=0, \tag{43}$$

where $\hat{\mathbb{C}}^{\alpha\beta}_{ab}$ is a mixed-variant effective elastic modulus tensor. Applying our previous assumptions that $\mathbf{F}^{\mathbf{P}}$ does not affect the lattice state and acts uniformly over Y, Eq. (43) becomes

$$J^{P-1}F^{P-1B}_{.\alpha}\frac{\partial}{\partial Y^B}\left(\hat{\mathbb{C}}^{\alpha\beta}_{ab}(F^b_{.A}-\delta^b_{.\chi}F^{P\ \chi}_{.A})\right)F^{P-1A}_{.\beta}=0. \tag{44}$$

Next, from the deformation gradient expression given by the first of Eq. (15), we have

$$-F^{P-1B}_{.\alpha}\frac{\partial\hat{\mathbb{C}}^{\alpha\beta}_{ab}}{\partial Y^B}\left(\frac{\partial\overline{u}^b}{\partial X^A}+\delta^b_{.A}-\delta^b_{.\chi}F^{P\chi}_{.A}\right)F^{P-1A}_{.\beta}=F^{P-1B}_{.\alpha}\frac{\partial}{\partial Y^B}\left(\hat{\mathbb{C}}^{\alpha\beta}_{ab}\frac{\partial\tilde{v}^b}{\partial Y^A}\right)F^{P-1A}_{.\beta}. \tag{45}$$

Our immediate goal is to express Eq. (45) in terms of atomistic and macroscopic displacements. Invoking the chain rule gives

$$\frac{\partial}{\partial\tilde{Z}^\alpha_{\langle j\rangle}}=\frac{\partial Y^A}{\partial\tilde{Z}^\alpha_{\langle j\rangle}}\frac{\partial}{\partial Y^A}=\overline{F}^{P-1A}_{\langle j\rangle\alpha}\frac{\partial}{\partial Y^A}, \tag{46}$$

where the linear operator $\overline{F}^{P-1A}_{\langle j\rangle\alpha}$ measures the change in intermediate atomic position of atom j with respect to a change in reference coordinates. Using Eq. (46) in the left-hand side of Eq. (45), we assume

$$\begin{aligned}F^{P-1B}_{.\alpha}\frac{\partial\hat{\mathbb{C}}^{\alpha\beta}_{ab}}{\partial Y^B}\left(\frac{\partial\overline{u}^b}{\partial X^A}+\delta^b_{.A}-\delta^b_{.\chi}F^{P\chi}_{.A}\right)F^{P-1A}_{.\beta}&\to\frac{\partial\hat{\mathbb{C}}^{\alpha\beta}_{ab}}{\partial\tilde{Z}^\alpha_{\langle j\rangle}}\left(\frac{\partial\overline{u}^b}{\partial X^A}+\delta^b_{.A}-\delta^b_{.\chi}F^{P\chi}_{.A}\right)F^{P-1A}_{.\beta}\\&=\frac{\partial^2\tilde{\Psi}}{\partial q^a_{\langle j\rangle}\partial F^{Lb}_{.\beta}}\left(\frac{\partial\overline{u}^b}{\partial X^A}+\delta^b_{.A}-\delta^b_{.\chi}F^{P\chi}_{.A}\right)F^{P-1A}_{.\beta}=-\mathscr{D}^{\beta}_{\langle j\rangle ab}\left(\frac{\partial\overline{u}^b}{\partial X^A}+\delta^b_{.A}-\delta^b_{.\chi}F^{P\chi}_{.A}\right)F^{P-1A}_{.\beta},\end{aligned} \tag{47}$$

and for the right-hand side of Eq. (45), rigorous for small atomic perturbations $\tilde{v}^a_{\langle m\rangle}$,

$$F^{P-1B}_{.\alpha}\frac{\partial}{\partial Y^B}\left(\hat{\mathbb{C}}^{\alpha\beta}_{ab}\frac{\partial\tilde{v}^b}{\partial Y^A}\right)F^{P-1A}_{.\beta}\to\frac{\partial}{\partial\tilde{Z}^\alpha_{\langle j\rangle}}\left(\hat{\mathbb{C}}^{\alpha\beta}_{ab}\frac{\partial\tilde{v}^b_{\langle k\rangle}}{\partial\tilde{Z}^\beta_{\langle j\rangle}}\right)=\frac{\partial^2\tilde{\Psi}}{\partial q^a_{\langle k\rangle}\partial q^b_{\langle j\rangle}}\tilde{v}^b_{\langle k\rangle}=\mathscr{H}_{\langle jk\rangle ab}\tilde{v}^b_{\langle k\rangle}. \tag{48}$$

In Eqs. (47) and (48), the "→" notation denotes the transformation steps $\tilde{v}^b\to\tilde{v}^b_{\langle k\rangle}$ and $\overline{F}^{P\ \alpha}_{\langle k\rangle A}F^{P-1A}_{.\beta}\to\delta^\alpha_{.\beta}$, the latter implying that $\overline{F}^{P-1A}_{\langle k\rangle\alpha}$ acts uniformly over all atoms k within each periodic cell. Using Eqs. (47) and (48), the fine scale equilibrium equation (42) finally becomes

$$\mathscr{D}^{\beta}_{\langle j\rangle ab}\left(\frac{\partial \bar{u}^b}{\partial X^A} + \delta^b_{.A} - \delta^b_{.\chi}F^{P\chi}_{.A}\right)F^{P-1A}_{.\beta} = \mathscr{H}_{\langle jk\rangle ab}\tilde{v}^b_{\langle k\rangle}, \tag{49}$$

where $\mathscr{D}^{\beta}_{\langle j\rangle ab} = -\partial^2\tilde{\Psi}/\partial q^a_{\langle j\rangle}\partial F^{Lb}_{.\beta}$ and the Hessian matrix $\mathscr{H}_{\langle jk\rangle ab} = \partial^2\tilde{\Psi}/\partial q^a_{\langle k\rangle}\partial q^b_{\langle j\rangle}$. In subsequent calculations, Eq. (49) is solved for the (atomic) inner displacements $\tilde{v}^b_{\langle k\rangle}$. Notice that for the particular case of an elastic (as opposed to elastic–plastic) material with defects, we have the conditions $\mathbf{F} = \mathbf{F^L}$, $\mathbf{F^P} = \mathbf{1}$, $\tilde{\Psi}(\mathbf{F^L}, \tilde{\xi}) \to \Psi(\mathbf{F}, \tilde{\xi})$, $\mathscr{D}^{B}_{\langle j\rangle ab} = -\partial^2\Psi/\partial q^a_{\langle j\rangle}\partial F^b_{.B}$, $\mathscr{H}_{\langle jk\rangle ab} = \partial^2\Psi/\partial q^a_{\langle j\rangle}\partial q^b_{\langle k\rangle}$, and Eq. (49) becomes equivalent to the original proposition of Chung and Namburu (2003), i.e.,

$$\mathscr{D}^{A}_{\langle j\rangle ab}\left(\frac{\partial \bar{u}^b}{\partial X^A}\right) = \mathscr{H}_{\langle jk\rangle ab}\tilde{v}^b_{\langle k\rangle}. \tag{50}$$

Now we reconsider coarse-scale Eq. (31), assuming that $\tilde{\mathbf{v}}$ is known from solution of Eq. (49). The left-hand side of Eq. (31) can be written as

$$\begin{aligned}&\frac{1}{Y}\int_Y\int_V J^{P-1}F^{P-1B}_{.\alpha}\frac{\partial\tilde{\Psi}}{\partial F^{La}_{.\alpha}}\frac{\partial(\delta\bar{u}^a)}{\partial X^B}\,\mathrm{d}V\,\mathrm{d}Y\\ &\quad=\frac{1}{Y}\int_Y\int_V J^{P-1}F^{P-1B}_{.\alpha}\hat{\mathbb{C}}^{\beta\alpha}_{ba}\left(\frac{\partial\bar{u}^b}{\partial X^A}+\frac{\partial\tilde{v}^b}{\partial Y^A}+\delta^b_{.A}-\delta^b_{.\chi}F^{P\chi}_{.A}\right)F^{P-1A}_{.\beta}\frac{\partial(\delta\bar{u}^a)}{\partial X^B}\,\mathrm{d}V\,\mathrm{d}Y,\end{aligned} \tag{51}$$

where fine scale perturbations and atomic positions affect $F^b_{.A}$ and $\hat{\mathbb{C}}^{\alpha\beta}_{ab}$ through Eqs. (15) and (39), respectively, and hence influence the macroscopic response. Following Eqs. (46)–(49), we may write

$$\hat{\mathbb{C}}^{\beta\alpha}_{ba}\frac{\partial\tilde{v}^b}{\partial Y^A}F^{P-1A}_{.\beta} \to \hat{\mathbb{C}}^{\beta\alpha}_{ba}\frac{\partial\tilde{v}^b_{\langle j\rangle}}{\partial\tilde{Z}^{\beta}_{\langle j\rangle}} = \frac{\partial^2\tilde{\Psi}}{\partial q^b_{\langle j\rangle}\partial F^{La}_{.\alpha}}\tilde{v}^b_{\langle j\rangle} = -\mathscr{D}^{\alpha}_{\langle j\rangle ba}\tilde{v}^b_{\langle j\rangle}, \tag{52}$$

such that Eq. (31) becomes

$$\begin{aligned}&\frac{1}{Y}\int_Y\int_V \overline{\mathbb{C}}^{AB}_{ba}\left(\frac{\partial\bar{u}^b}{\partial X^A}+\delta^b_{.A}-\delta^b_{.\chi}F^{P\chi}_{.A}\right)\frac{\partial(\delta\bar{u}^a)}{\partial X^B}\,\mathrm{d}V\,\mathrm{d}Y\\ &\quad=\int_{\partial V}T^a g_{ab}\delta\bar{u}^b\,\mathrm{d}A+\int_V B^a g_{ab}\delta\bar{u}^b\,\mathrm{d}V+\frac{1}{Y}\int_Y\int_V\overline{\mathscr{D}}^{B}_{\langle j\rangle ba}\tilde{v}^b_{\langle j\rangle}\frac{\partial(\delta\bar{u}^a)}{\partial X^B}\,\mathrm{d}V\,\mathrm{d}Y.\end{aligned} \tag{53}$$

where $\overline{\mathbb{C}}^{AB}_{ba} = J^{P-1}F^{P-1B}_{.\alpha}\hat{\mathbb{C}}^{\beta\alpha}_{ba}F^{P-1A}_{.\beta}$ and $\overline{\mathscr{D}}^{B}_{\langle j\rangle ba} = J^{P-1}F^{P-1B}_{.\alpha}\mathscr{D}^{\alpha}_{\langle j\rangle ba}$. Later, Eq. (53) will be converted to a finite-element equation applied over spatially discretized domain V.

As is clear from relations (47) and (48), the theory effectively equates $\tilde{v}^a$ and $\tilde{v}^a_{\langle k\rangle}$, implying two main assumptions. Firstly, neglecting the change in configurations, the atomic discrete degrees-of-freedom $\tilde{v}^a_{\langle k\rangle}$ are assumed to be equivalent to the fine scale continuum analog from classical two-scale homogenization theory, $\tilde{v}^a$. This assertion was made in earlier papers by Chung and co-workers (Chung and Namburu, 2003; Chung, 2004), and was further modified for efficient computer implementation by the present authors (Chung and Clayton, 2006). It is a fundamental assumption made without mathematical proof. Physically, it implies that atomic deviations from the Cauchy–Born rule are equivalent to fine scale perturbations due to microstructure heterogeneity in the sense of two-scale continuum homogenization.

Secondly, $\tilde{v}^a$ is a spatial quantity in the two-scale continuum theory representing local perturbations from the reference state B_0, whereas $\tilde{v}^a_{\langle k \rangle}$ is a spatial quantity representing atomic perturbations from the intermediate configuration $\tilde{B}$. Since $\mathbf{F}^\mathbf{P}$ does not affect the underlying lattice or the atomic coordinates as discussed above, we assume that the perturbations from the reference state are the same as those from the intermediate state.

The manipulations in Eq. (47) effectively embed a deformation gradient (i.e., $\mathbf{F}^\mathbf{L}$) into the operator $\mathscr{D}^\beta_{\langle j \rangle ab}$. Hence the rightmost term of the macroscopic equation (53) implicitly involves gradients of the atomistic variable $\tilde{v}^b_{\langle j \rangle}$. This result follows from the two-scale mathematical homogenization approach presently used and embodies the features of weak convergence usually encountered for such methods (Nguetseng, 1989; Allaire, 1992), as discussed earlier. In practice and in contrast to many existing coupled multiscale approaches, the characteristic length scales in X (continuum) and Y (atomistic) are not necessarily identical, and therefore, no length scale-preserving displacement boundary conditions between the domains are required. Only the correlated inter-scale gradients are enforced in an average sense over each domain. We also note that Eqs. (49) and (53) are coupled in terms of solution variables $\tilde{v}$ and $\overline{u}$.

4.2. Inelastic fields and defect kinetics

Depending upon the fine scale physics representation, additional kinetic equations may be required in our framework in order to advance the plastic deformation gradient $\mathbf{F}^\mathbf{P}$ and internal variables $\tilde{\boldsymbol{\xi}}$. In the continuum description, these are written as

$$\dot{\mathbf{F}}^\mathbf{P} = \dot{\mathbf{F}}^\mathbf{P}(\mathbf{F}, \mathbf{F}^\mathbf{P}, \tilde{\boldsymbol{\xi}}, \theta), \tag{54}$$

$$\dot{\tilde{\boldsymbol{\xi}}} = \dot{\tilde{\boldsymbol{\xi}}}(\mathbf{F}, \mathbf{F}^\mathbf{P}, \tilde{\boldsymbol{\xi}}, \theta), \tag{55}$$

assuming that instantaneous rates depend upon the thermodynamic state described by the first of Eq. (23). When a finite-temperature atomistic description is invoked at the fine scale, Eq. (54) may not be needed a priori, as the plastic velocity gradient can conceivably be expressed in terms of the flux of mobile dislocations. One can formulate an approximate expression for the rate of the mapping $\dot{\mathbf{F}}^\mathbf{P}$ in terms of the dislocation velocity, line length, and orientation (Teodosiu, 1969). A similar approach has been used by Zbib and co-workers in the context of discrete dislocation plasticity (Zbib and de la Rubia, 2002). Conceivably, our approach could be modified such that $\dot{\mathbf{F}}^\mathbf{P}$ could be extracted in such a manner directly from the atomistics, though it is a nontrivial task to precisely define the location of the dislocation line in the atomistic domain, and our method would need to be extended to account for dynamics in order to track the dislocation velocity, as no time scale enters the present static formulation. One cannot construct an explicit formula for the tangent map $\mathbf{F}^\mathbf{P}$ itself unless the dislocation geometry and velocity are constant over the time history of deformation. In the present implementation, Eq. (54) is needed as the physics of thermally activated dislocation glide are not adequately addressed by our static calculations at the fine scale. Relation (55) controls, for example, rates of defect generation or annihilation, in instances when such kinetics are not modeled directly at the fine scale, as is again the case in the present zero-temperature atomistic implementation. Simple, yet specific, forms of Eqs. (54) and (55) follow in the discussion of numerical results in Section 6.3.

5. Numerical implementation

As the material response is nonlinear in the presence of defects, an iterative scheme is employed for application of our computational method to deforming crystals. The initial-boundary value problem consists of the macroscopic domain V, discretized here into standard finite elements. The integration point of each element in turn represents a microscopic unit cell of volume Y, consisting of $\mathbb{N}$ atoms subjected to periodic fine scale boundary conditions. Defects such as dislocations may be present in the initial configuration, at $t = 0$, accompanying the standard assumption $\mathbf{F}^{\mathbf{P}}_{t=0} = \mathbf{1}$. Details of the iterative algorithm are listed below. In what follows, we denote by Δt the time increment over which a numerical integration cycle takes place, and $\Delta\bar{\mathbf{u}}$ and $\Delta\tilde{\mathbf{v}}$ denote increments in macro- and micro-displacement vectors over Δt.

1. Incrementally increase the applied load.
   - (a) Begin element loop, for each element level integration point:
     - (i) Update the coarse-scale deformation gradient $\overline{\mathbf{F}}$.
     - (ii) Compute the lattice deformation gradient $\mathbf{F}^{\mathbf{L}} = \mathbf{F}\mathbf{F}^{\mathbf{P}-1}$, where at the coarse scale, $\overline{\mathbf{F}}$ and $\mathbf{F}$ are assumed effectively equivalent.
     - (iii) Update atomic positions via Eq. (37), with $\tilde{\mathbf{v}} = \mathbf{0}$ initially and $\overline{F}^{La}_{\langle jk\rangle\alpha} = F^{La}_{.\alpha}\delta_{\langle jk\rangle}$.
     - (iv) Calculate the Hessian $\mathscr{H}_{\langle jk\rangle ab} = \partial^2\tilde{\Psi}/\partial q^a_{\langle k\rangle}\partial q^b_{\langle j\rangle}$ and $\mathscr{D}_{\langle j\rangle ab} = \partial^2\tilde{\Psi}/\partial q^a_{\langle j\rangle}\partial F^{Lb}_{.\beta}$ from the atomistic potential energy $\tilde{E}$ (for example, see later Eqs. (70)–(71)).
     - (v) Apply periodic boundary conditions and solve fine scale Eq. (49) for $\Delta\tilde{\mathbf{v}}$:

$$\mathscr{D}^{\beta}_{\langle j\rangle ab}\left(\frac{\partial(\Delta\bar{u}^b)}{\partial X^A} + \delta^b_{.A} - \delta^b_{.\chi}F^{P\chi}_{.A}\right)F^{P-1A}_{.\beta} = \mathscr{H}_{\langle jk\rangle ab}(\Delta\tilde{v}^b_{\langle k\rangle}), \tag{56}$$

       where $\Delta\bar{\mathbf{u}}$ is known at present following the update of $\overline{\mathbf{F}}$ of step (i) above.
     - (vi) Repeat steps (iii), (iv), and (v) above until $\Delta\tilde{\mathbf{v}} \to \mathbf{0}$ on successive counts.
     - (vii) Compute $\hat{\mathbb{C}}^{\alpha\beta}_{ab} = \partial^2\tilde{\Psi}/\partial F^{La}_{.\alpha}\partial F^{Lb}_{.\beta}$ from the atomic energy $\tilde{E}$ (see later Eq. (72)).
     - (viii) Calculate the effective elastic stiffness $\overline{\mathbb{C}}^{AB}_{ba} = J^{P-1}F^{P-1B}_{.\alpha}\hat{\mathbb{C}}^{\beta\alpha}_{ba}F^{P-1A}_{.\beta}$ and the quantity $\overline{\mathscr{D}}^{B}_{\langle j\rangle ba} = J^{P-1}F^{P-1B}_{.\alpha}\mathscr{D}^{\alpha}_{\langle j\rangle ba}$.
   - (b) Compute and assemble the finite element equations. In discretized incremental form, the left-hand side of (53) becomes

$$\begin{aligned}&\frac{1}{Y}\int_Y\int_V \overline{\mathbb{C}}^{AB}_{ba}\left[\frac{\partial\Delta\bar{u}^b}{\partial X^A} + \delta^b_{.A} - \delta^b_{.\chi}F^{P\chi}_{.A}\right]\frac{\partial(\Delta\bar{u}^a)}{\partial X^B}\,\mathrm{d}V\,\mathrm{d}Y\\ &\quad\to \int_V \overline{\mathbb{C}}^{AB}_{ba}\left[\frac{\partial}{\partial X^A}(\underline{N}^b_c\Delta\underline{u}^c) + \delta^b_{.A} - \delta^b_{.\chi}F^{P\chi}_{.A}\right]\frac{\partial}{\partial X^B}(\underline{N}^a_d\Delta\underline{u}^d)\,\mathrm{d}V,\end{aligned} \tag{57}$$

     where $\underline{\mathbf{N}}$ is the element shape function and $\Delta\underline{\mathbf{u}}$ is the nodal displacement increment. Similarly, the right-hand side of (53) can be written

$$\begin{aligned}&\int_{\partial V}\Delta T^a g_{ab}\Delta\bar{u}^b\,\mathrm{d}A + \int_V \Delta B^a g_{ab}\Delta\bar{u}^b\,\mathrm{d}V + \frac{1}{Y}\int_Y\int_V \overline{\mathscr{D}}^{B}_{\langle j\rangle ba}\tilde{v}^b_{\langle j\rangle}\frac{\partial(\Delta\bar{u}^a)}{\partial X^B}\,\mathrm{d}V\,\mathrm{d}Y\\ &\quad\to \int_{\partial V}\Delta T^a g_{ab}\underline{N}^b_c\Delta\underline{u}^c\,\mathrm{d}A + \int_V \Delta B^a g_{ab}\underline{N}^b_c\Delta\underline{u}^c\,\mathrm{d}V\end{aligned}$$

$$+ \int_V \overline{\mathscr{D}}^{B}_{\langle j\rangle ba} \tilde{v}^{b}_{\langle j\rangle} \frac{\partial}{\partial X^B} (\underline{N}^a_c \Delta \underline{u}^c)\, \mathrm{d}V. \tag{58}$$

Combining (57) and (58) then gives

$$\begin{aligned} \Delta\underline{u}^c \left[\int_V \frac{\partial(\underline{N}^b_c)}{\partial X^A} \overline{\mathbb{C}}^{AB}_{ba} \frac{\partial(\underline{N}^a_d)}{\partial X^B}\, \mathrm{d}V \right] \Delta\underline{u}^d & \\ = \Delta\underline{u}^c \int_{\partial V} \Delta T^a g_{ab} \underline{N}^b_c\, \mathrm{d}A + \Delta\underline{u}^c \int_V \Delta B^a g_{ab} \underline{N}^b_c\, \mathrm{d}V & \\ + \Delta\underline{u}^c \int_V \left[\overline{\mathscr{D}}^{B}_{\langle j\rangle ba} \tilde{v}^{b}_{\langle j\rangle} + \overline{\mathbb{C}}^{AB}_{ba} (\delta^b_{.A} - \delta^b_{.\chi} F^{P\chi}_{.A}) \right] \frac{\partial(\underline{N}^a_c)}{\partial X^B}\, \mathrm{d}V, & \end{aligned} \tag{59}$$

which can be reduced upon taking the first variation to the finite element equation

$$\underline{K}_{cd} \Delta\underline{u}^d = \underline{T}_c + \underline{B}_c + \underline{D}_c. \tag{60}$$

Solution of Eq. (60) involves

(i) Compute $\underline{K}_{cd} = \sum_e \int_{\underline{V}} [\partial(\underline{N}^b_c)/\partial X^A] \overline{\mathbb{C}}^{AB}_{ba} [\partial(\underline{N}^a_d)/\partial X^B]\, \mathrm{d}\,\underline{V}$, where summation runs over e finite elements of volume $\underline{V}$.

(ii) Compute $\underline{T}\ _c = \sum_e \int_{\partial\,\underline{V}} \Delta T^a g_{ab} \underline{N}^b_c\, \mathrm{d}\,\underline{A}$, with $\underline{A}$ the external surface area of element e, with ΔT^a the incremental traction vector.

(iii) Compute $\underline{B}\ _c = \sum_e \int_{\underline{V}} \Delta B^a g_{ab} \underline{N}^b_c\, \mathrm{d}\,\underline{V}$, with ΔB^a the incremental body force vector.

(iv) Compute $\underline{D}_c = \sum_e \int_{\underline{V}} [\overline{\mathscr{D}}^{B}_{\langle j\rangle ba} \tilde{v}^{b}_{\langle j\rangle} + \overline{\mathbb{C}}^{AB}_{ba} (\delta^b_{.A} - \delta^b_{.\chi} F^{P\chi}_{.A})][\partial(\underline{N}^a_c)/\partial X^B]\, \mathrm{d}\,\underline{V}$, with $\tilde{\mathbf{v}}$ and $\overline{\mathbb{C}}^{AB}_{ba}$ both found from step 1(a).

(v) Invert Eq. (60) and solve for $\Delta\underline{u}^d$, i.e.

$$\Delta\,\underline{\mathbf{u}} = \underline{\mathbf{K}}^{-1}(\underline{\mathbf{T}} + \underline{\mathbf{B}} + \underline{\mathbf{D}}). \tag{61}$$

(c) Iterate to step 1(a) until $\Delta\underline{\mathbf{u}}_{n+1} - \Delta\underline{\mathbf{u}}_n \to \mathbf{0}$, where n and $n+1$ denote iterations.

2. Update the total nodal displacement field $\underline{\mathbf{u}}_{t+\Delta t} = \underline{\mathbf{u}}_t + \Delta\,\underline{\mathbf{u}}$.
3. Project forward the intermediate configuration ($\mathbf{F}^{\mathbf{P}}$ and defect arrangement $\tilde{\boldsymbol{\xi}}$) for the next increment at each element integration point (i.e. unit cell), based on the current local state.
4. Return to step 1 until final load is achieved.

No problems are introduced in our approach due to the fact that the field $\mathbf{F}^{\mathbf{P}}$ is incompatible, i.e., that $(F^P)^{\alpha}_{.A,B} \neq (F^P)^{\alpha}_{.B,A}$, in general. In continuum crystal plasticity theories, the mapping $\mathbf{F}^{\mathbf{P}}$ is generally not required to be compatible, and in fact, the skew-symmetric gradient of $\mathbf{F}^{\mathbf{P}}$ measuring its nonintegrability is often associated with geometrically necessary dislocation density tensor (Gurtin, 2002). In the unit cell calculations presented here, $\mathbf{F}^{\mathbf{P}}$ is imposed uniformly over each cell, and $\mathbf{F}^{\mathbf{L}}$ includes the effects of the fine scale perturbation $\tilde{v}$, except in the first iteration of the numerical procedure described above, where the Born assumption is used as the initial guess for updating the atomic coordinates. We only consider isolated unit cells in the applications that follow, but the theory invokes no restrictions on how $\mathbf{F}^{\mathbf{P}}$ or its gradients can vary from cell to neighboring cell on the coarse scale.

6. Application: defects in tungsten

In the present work our formulation is applied to study the mechanical behavior of pure tungsten (W), a BCC transition metal of relatively high mass density. Its combination of high density and strength make it an attractive material for use in defense applications such as ordnance (Zhou and Clifton, 1997; Clayton, 2005). The potential energy function describing atomistic interactions in W is discussed in Section 6.1. Numerical results for illustrative boundary value problems then follow. In Section 6.2, these describe the nonlinear elastic response of a deforming W crystal containing (i) vacancies, (ii) screw dislocations of like sign and screw dislocation dipoles, and (iii) low-angle twist boundaries. Then in Section 6.3 we address the energetic and stiffness properties of a plastically deforming single crystal containing screw dislocations.

6.1. Atomistic potential: tungsten

We employ an empirical $\mathbb{N}$-body potential specifically developed for transition metals (Finnis and Sinclair, 1984) in order to estimate the free-energy potential $\tilde{\Psi}$ of Eq. (39). Duesberry and Vitek (1998) exercised the Finnis–Sinclair potential to model screw dislocation core structures, construct generalized stacking fault energy surfaces, and predict plastic slip anisotropy (i.e. tension–compression asymmetry in the yield function) in multiple BCC transition metals, including W. Liu et al. (2004) used the Finnis–Sinclair potential for studying edge dislocation glide in W and molybdenum, and Tian and Woo (2004) invoked a variation of this potential (Ackland and Thetford, 1987) to simulate screw dislocation motion in W. Please note that while the choice of atomistic potential is extremely important in order to ensure the appropriate physics are captured, our primary interest in the present research effort is development of the multiscale homogenization technique, which may be exercised using any available potential energy function of form (39), or more generally, for any crystalline material for which atomic energy, force, and stiffness are known (e.g., in terms of tabulated values obtained from more refined electronic structure calculations). The particular potential used here (Finnis and Sinclair, 1984) was selected because of its apparently adequate capability for describing dislocation energetics in W, as reported in the above-mentioned papers. The total potential energy $\tilde{E}$ of a set of atoms at positions $\{\mathbf{z}_{\langle j\rangle}\}$, for $j = 1, 2, \ldots, \mathbb{N}$ is given by the sum

$$\tilde{E} = \tilde{E}_N + \tilde{E}_P \tag{62}$$

where $\tilde{E}_N$ is the $\mathbb{N}$-body term that is a function of the superposition of the local electronic charge density ρ, the latter obtained from a further superposition of atomic charge densities, ϕ. Also in Eq. (62), $\tilde{E}_P$ is a pair potential that models core–core interactions. The $\mathbb{N}$-body term is constructed as

$$\tilde{E}_N = -\Lambda \sum_{\langle j\rangle} f(\tilde{\rho}_{\langle j\rangle}), \tag{63}$$

where

$$f(\tilde{\rho}_{\langle j\rangle}) = \sqrt{\tilde{\rho}_{\langle j\rangle}}, \quad \tilde{\rho}_{\langle j\rangle} = \sum_{k} \tilde{\phi}(r_{\langle j\backslash k\rangle}) \tag{64}$$

is always non-negative and real,

$$r_{\langle j\backslash k\rangle} = |\mathbf{r}_{\langle j\backslash k\rangle}| = |\mathbf{z}_{\langle k\rangle} - \mathbf{z}_{\langle j\rangle}|, \tag{65}$$

$$\tilde{\phi}(r) = \begin{cases} (r-d)^2, & r \leqslant d, \\ 0, & r > d, \end{cases} \tag{66}$$

and Λ is an empirical constant. The adjustable parameter d represents a cut-off zone for superposition of local charge densities. For BCC tungsten with lattice parameter a, the value of d is chosen to lie between the second- and third-nearest neighbors, i.e. $a < d < a\sqrt{2}$, for computational convenience. The pair potential $\tilde{E}_P$ is formed as

$$\tilde{E}_P = \frac{1}{2} \sum_{j,k,j \neq k} \tilde{\psi}(r_{\langle j \backslash k \rangle}) \tag{67}$$

where $\tilde{\psi}$ is of the polynomial form

$$\tilde{\psi}(r) = \begin{cases} (r-c)^2(c_0 + c_1 r + c_2 r^2), & r \leqslant c, \\ 0, & r > c, \end{cases} \tag{68}$$

with empirical constants c_0, c_1, and c_2. The parameter c, also adjustable, is presently assigned a value between the second- and third-nearest-neighbor distances. Finnis and Sinclair (1984) obtained the other constants via calibration to experimental data on macroscopic elastic properties; Tables 1 and 2 list the experimental and fitted parameters, respectively.

Notice that $\tilde{E}$ is the total energy of $\mathbb{N}$ atoms in the fine scale unit cell. The Helmholtz free energy density in a continuum sense, $\tilde{\Psi}$, is related to $\tilde{E}$ as

$$\tilde{\Psi} = \tilde{U} - \tilde{\eta}\theta = \frac{1}{\mathbb{N}} \tilde{E}, \tag{69}$$

where $\tilde{U}$ is the continuum internal energy, $\tilde{\eta}$ is the continuum entropy per unit volume, and θ is the absolute thermodynamic temperature of the system, which we assume is zero in the

Table 1
Experimental lattice quantities for W

A	Lattice parameter (Å)	3.1652
U^c	Cohesive energy (eV)	−8.90
C_{11}	Elastic constant (GPa)	522.4
C_{12}	Elastic constant (GPa)	204.4
C_{44}	Rhombohedral shear modulus (GPa)	160.6
C'	Tetragonal shear modulus (GPa)	159.0
B	Bulk modulus (GPa)	310.4
P_c	Cauchy pressure $= \frac{1}{2}(C_{12} - C_{44})$	21.9

Table 2
Constants for EAM potential (W)

d (Å)	4.40024
Λ (eV)	1.896373
c (Å)	3.25
c_0	47.1346499
c_1	−33.7665655
c_2	6.2541999

last of Eq. (69) for the present case of molecular statics simulations, such that $\mathbb{N}\tilde{U} = \tilde{E}$. Substitution of Eq. (69) into earlier definitions then gives

$$\mathscr{H}_{\langle jk\rangle ab} = \frac{\partial^2 \tilde{\Psi}}{\partial q^a_{\langle k\rangle} \partial q^b_{\langle j\rangle}} = \frac{1}{\mathbb{N}}\left[\frac{\partial^2(\tilde{E}_N + \tilde{E}_P)}{\partial q^a_{\langle k\rangle}\partial q^b_{\langle j\rangle}}\right], \tag{70}$$

$$\mathscr{D}^{\beta}_{\langle j\rangle ab} = -\frac{\partial^2 \tilde{\Psi}}{\partial q^a_{\langle j\rangle}\partial F^{Lb}_{.\beta}} = -\frac{1}{\mathbb{N}}\frac{\partial^2(\tilde{E}_N + \tilde{E}_P)}{\partial q^a_{\langle j\rangle}\partial q^c_{\langle k\rangle}}\frac{\partial q^c_{\langle k\rangle}}{\partial F^{Lb}_{.\beta}}, \tag{71}$$

$$\hat{\mathbb{C}}^{\alpha\beta}_{ab} = \frac{\partial^2 \tilde{\Psi}}{\partial F^{La}_{.\alpha}\partial F^{Lb}_{.\beta}} = \frac{1}{\mathbb{N}}\frac{\partial^2(\tilde{E}_N + \tilde{E}_P)}{\partial q^c_{\langle j\rangle}\partial q^d_{\langle k\rangle}}\frac{\partial q^c_{\langle j\rangle}}{\partial F^{La}_{.\alpha}}\frac{\partial q^d_{\langle k\rangle}}{\partial F^{Lb}_{.\beta}}, \tag{72}$$

where from relations (34)–(38) with $\overline{F}^{La}_{\langle jk\rangle\alpha} = F^{La}_{.\alpha}\delta_{\langle jk\rangle}$, to first order,

$$\frac{\partial r^c_{\langle j\backslash k\rangle}}{\partial F^{La}_{.\alpha}} = \tilde{R}^{\alpha}_{\langle j\backslash k\rangle}\delta^c_{.a}, \quad \frac{\partial q^b_{\langle j\rangle}}{\partial F^{La}_{.\alpha}} = \tilde{Z}^{\alpha}_{\langle j\rangle}\delta^b_{.a}. \tag{73}$$

Derivatives of $\tilde{E}$ with respect to atomic displacements $q^a_{\langle j\rangle}$ are listed by Finnis and Sinclair (1984) and are not repeated here. In our numerical implementation, expressions (70)–(73) are evaluated analytically and subsequently used in Eqs. (56) and (60).

6.2. Multiscale nonlinear elasticity with defects

Here we report results of simulations of unit cells containing various numbers of atoms configured to represent several classes of crystal defects. Essentially, we perform calculations in which the tangent stiffness of a single Lagrangian finite element integration point is determined by the microscopic (i.e., atomistic) response. A sample atomistic unit cell representative of all calculations described in the present work is illustrated in Fig. 3. The BCC unit cell is a rectangle of dimensions $L_1 \times L_2 \times L_3 = a\sqrt{3}N_1 \times a\sqrt{6}N_2 \times a\sqrt{2}N_3$, where N_1, N_2, and N_3 are respectively the number of repeating planes stacked in the [1 1 1]-, [1 1 $\overline{2}$]-, and [1 $\overline{1}$ 0]-directions. Periodic boundary conditions are applied along all faces of the unit cell in the usual manner (cf. Vitek, 1976), such that atoms exiting the unit cell during the calculation are mapped back into the cell on the opposite face, thereby preserving the total mass of the system.

In the present section (6.2), we examine the response of W containing defects under the conditions of null dislocation flux, i.e. the local deformation gradient $\mathbf{F} = \mathbf{F^L} = \overline{\mathbf{F}}\tilde{\mathbf{F}}$ in the context of Eq. (33) and Fig. 2. Our goal here is to examine aspects of material behavior that could be used subsequently in stand-alone continuum theories, in particular details associated with stored energy of defect fields and the effects of applied deformations on elasticity and stored energy, for various fixed defect concentrations. Please recall that our approach is presently restricted to static calculations, i.e., $\theta = 0\,\mathrm{K}$, as we have yet to develop kinetics relations and scaling laws for finite temperature response. Nonetheless, one may still draw conclusions, at least in a qualitative sense, regarding stress and energetics associated with dislocation behavior in BCC metals in the context of lattice statics calculations (Vitek, 1976; Duesberry and Vitek, 1998). A standard trend in the literature has been development of such scaling methods for the purely mechanical problem before extending to the finite temperature regime (Dupuy et al.,

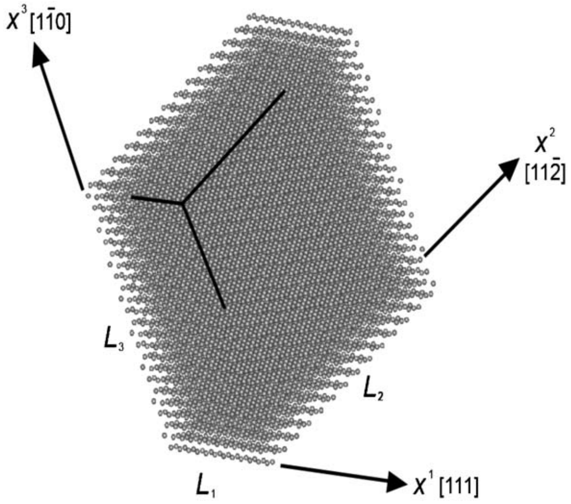

Fig. 3. Atomistic scale unit cell for perfect BCC lattice.

2005). Milstein and co-workers (Milstein and Chantasiriwan, 1998; Milstein et al., 2004) have analyzed the response of a number of metallic crystalline elements using molecular mechanics techniques (including lattice statics with the embedded atom method); nonlinear elastic moduli, void formation, and elastic instabilities were studied in these works, though periodic initial defect distributions and dislocations were not.

In the present set of calculations, initial atomic coordinates are found using a two-step procedure: first the linear-elastic solution for displacement field of the defect is applied to the atoms, then a conjugate gradient algorithm (Plimpton and Hendrickson, 1993) is used to transition the atomic positions to a stable local minimum energy state. Subsequently, the response to applied deformation is computed using our asymptotic homogenization scheme according to the numerical procedure described in Section 5. The applied (i.e., coarse-scale) deformation gradient field (in conjunction with fine scale periodicity) is uniaxial stretching in the [1 1 1]-direction (see Fig. 3) over a range of $1.000 \leqslant F_{11} \leqslant 1.025$, with the lateral edges fixed (covariant Cartesian notation is used here and in subsequent figures for simplicity, i.e. $\overline{F}^{1}_{.1} \to F_{11}$). We also compare the final configurations attained using our procedure with that of incremental energy minimization. In the latter approach, a small increment in the stretch field is first imposed uniformly over all atoms, and then a conjugate gradient program is used to update the atomic coordinates to the corresponding local minimum energy state. This process continues with a new set of conjugate gradient minimization iterations conducted upon application of each successive stretch increment until the final, fully deformed configuration is attained.

First we consider a point vacancy, as shown in Fig. 4(a). The initial configuration is constructed simply by removing the atom closest to the centroid of the unit cell. The defect density in this case is defined as the volume fraction of missing atoms, i.e., $\rho^{\mathrm{d}} = 1/\mathbb{N}$, where $\mathbb{N}$ is the total number of atoms prior to vacancy creation, ranging from 2016 to 32 256 among the simulations discussed here. Defect energy is shown in Fig. 4(b), defined

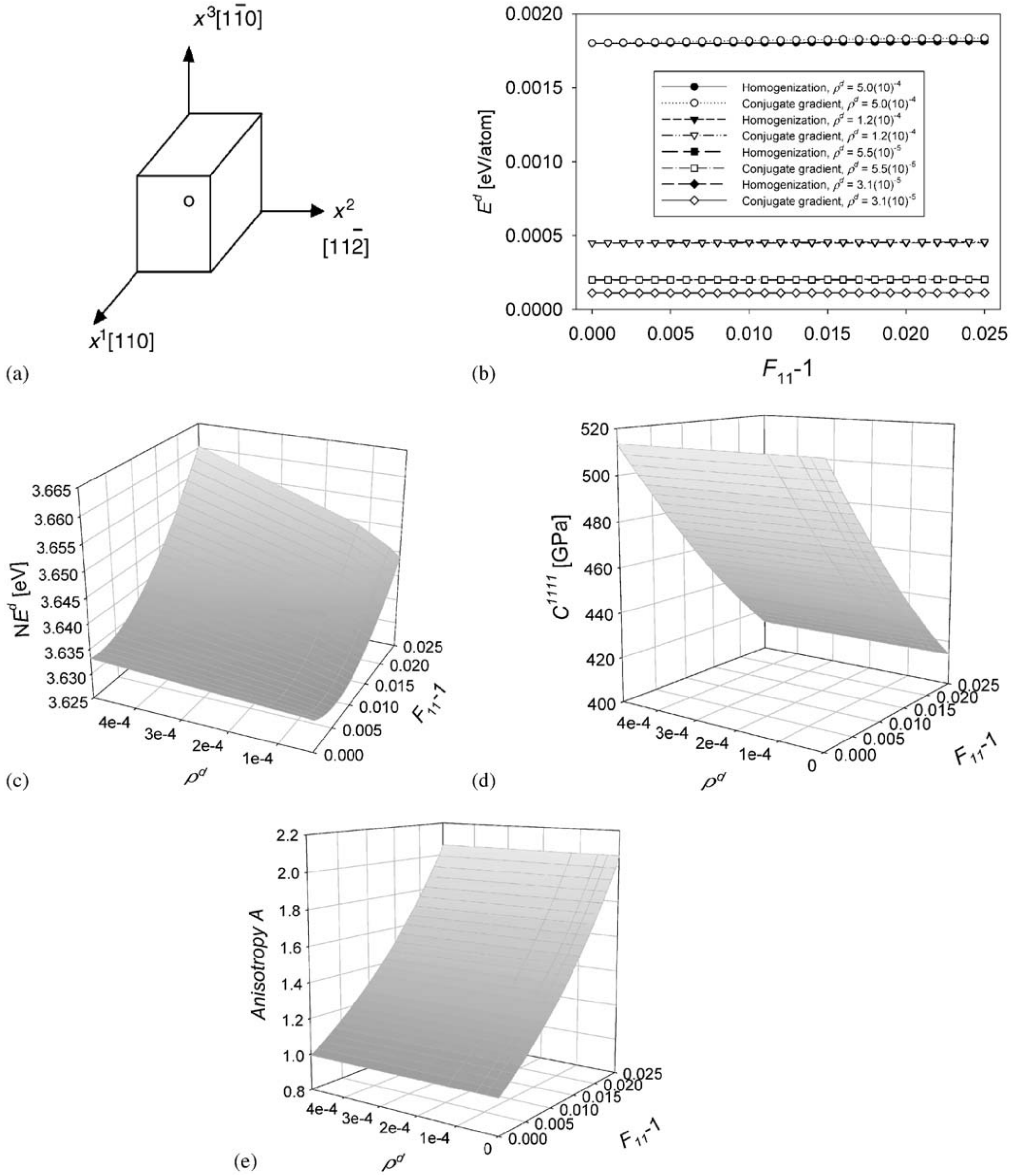

Fig. 4. Vacancy configuration (a), strain energy comparison between computational methods (b), defect energy (c), elastic stiffness (d), and Zener anisotropy (e).

on a per-atom basis as

$$E^{\mathrm{d}} = \frac{\tilde{E} - \overline{E}}{\mathbb{N}}, \tag{74}$$

where $\tilde{E}$ is the total potential energy of the system and $\overline{E}$ is the total potential energy of a perfect BCC W lattice of the same dimensions and same number of atoms (prior to vacancy formation), subjected to the same deformation boundary conditions. From Fig. 4(b), we see that our homogenization approach is validated in the sense that it predicts minimum energy atomic configurations that compare favorably with those obtained using incremental conjugate gradient minimization. In Fig. 4(c), the total defect energy $\mathbb{N}E^{\mathrm{d}}$ is shown. Schultz (1991) reported an experimental value of 3.6 eV for vacancy formation energy in W at null applied strain. Notice that the defect energy increases with applied stretch F_{11}. Shown in Fig. 4(d) is the elastic modulus component $C^{1111} = \hat{\mathbb{C}}_{11}^{11}$, computed via Eq. (72). Values decrease drastically with applied stretch, to around 80% of their original magnitudes at $F_{11} = 1.025$. In contrast, the defect density has little effect on C^{1111}, though this could be expected at such dilute vacancy concentrations as are considered here (i.e., porosities less than 0.1%). Fig. 4(c) shows the Zener anisotropy factor A, defined by (cf. Hirth and Lothe, 1982)

$$A = \frac{2C^{1212}}{C^{1111} - C^{1122}} = \frac{2\hat{\mathbb{C}}_{11}^{22}}{\hat{\mathbb{C}}_{11}^{11} - \hat{\mathbb{C}}_{12}^{12}}, \tag{75}$$

where the Cartesian contravariant notation is used in Fig. 4(c) and in the expression following the first equality in Eq. (75). Note that defect-free W is nominally isotropic at null deformation, i.e., $A = 1.00$, and that the anisotropy increases dramatically as the lattice is stretched. This result may in part be due to a limitation in the Finnis and Sinclair (1984) potential, whose parameters are calibrated to small-strain elastic moduli, although first-principles (i.e., quantum-mechanical) calculations have indicated a departure from isotropy in W at large pressures (Ruoff et al., 1998).

Regarding the vacancy concentrations considered here (ρ^{d} on the order of 10^{-4}), we note that such high concentrations would be unlikely to exist in commercially melt-grown pure single crystals, and that for very dilute concentrations (on the order of parts per million), the effects on the energetic and mechanical properties would apparently be quite small. However, for tungsten crystals and alloys generated from powder consolidation/compaction and sintering processes, even higher porosities on the order of several percent are not uncommon (cf. Yih and Wang, 1979). In such cases, the effects on properties would be substantial, perhaps orders of magnitude more so than the results listed here in Fig. 4. Such highly porous tungsten is used, for example, in electrical applications (Selcuk and Wood, 2005), where cyclic fatigue is of concern.

The response of W containing a periodic array of screw dislocations is investigated next. The defect configuration is illustrated in Fig. 5(a). The dislocation tangent line and burgers vector **b** are oriented along the [1 1 1]-direction and pass through the centroid of the unit cell, the latter having a magnitude of $b = |\mathbf{b}| = \sqrt{3}a/2$. Initial atomic positions are prescribed via the usual displacement field solution for a screw dislocation embedded in an infinite isotropic elastic body, i.e. $u = b\hat{\theta}/2\pi$, where $\hat{\theta}$ is an angular coordinate about the axis of the dislocation line. The scalar dislocation density is defined as the defect line length per unit reference volume, i.e., $\rho^{\mathrm{d}} = 1/(L_2 L_3)$. The defect energy per atom, defined as in Eq. (74) and shown in Fig. 5(b), is computed accurately by our homogenization scheme as is verified by the incremental conjugate gradient solutions. Furthermore, we see a linear increase in stored defect energy with applied deformation F_{11}, and a roughly linear increase in E^{d} with increasing dislocation density ρ^{d}. Gibeling and Nix (1980) discussed, from the standpoint of discrete dislocation modeling, how the strain energy supported by dislocations may be amplified by applied external deformations, and Clayton (2005)

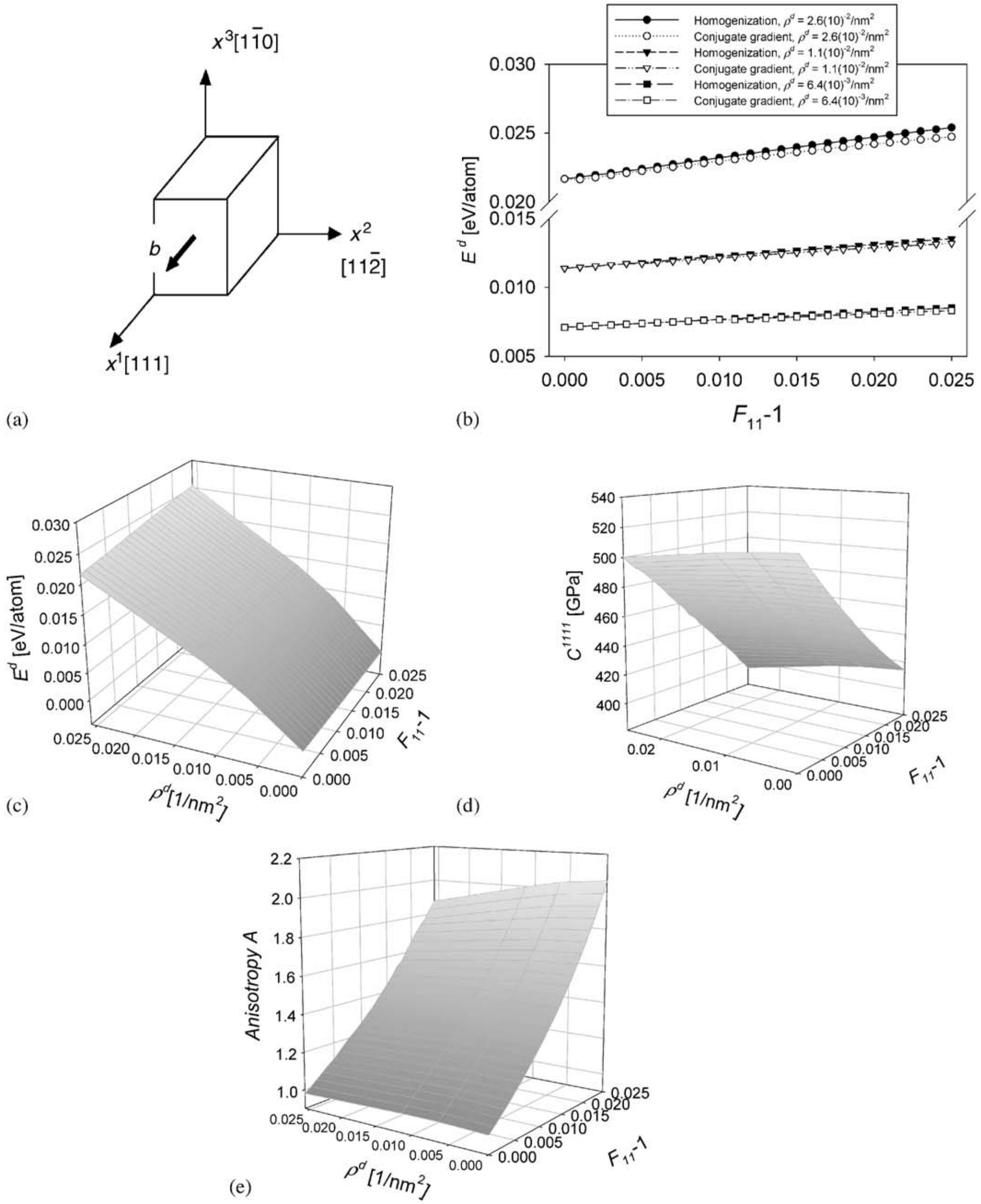

Fig. 5. Screw dislocation configuration (a), strain energy comparison between computational methods (b), defect energy (c), elastic stiffness (d), and Zener anisotropy (e).

assumed a linear dependence of stored elastic energy on dislocation density in a continuum crystal plasticity model of single crystalline W. Note that we are not attempting to compute isolated dislocation energies as has been the goal of previous studies (cf. Cai et al., 2003).

Instead, here we wish to include the effects of neighboring defects, thereby representing a distribution of lattice imperfections as would occur in a plastically deforming sample of material. Note also that a distribution of identically oriented dislocations produces a net (geometrically necessary) dislocation density tensor in the sense of Nye (1953), implying curvature in the lattice (see also Ashby, 1970). From Figs. 5(d) and (e), we see that the dislocation density tends to accelerate the decrement in stiffness value C^{1111} with increasing applied stretch, whereas the anisotropy A tends to be suppressed by increasing dislocation content as the stretch increases. In particular, at null applied strain, C^{1111} decreases from 514 to 500 GPa as the defect density is increased from 0 to 0.026/nm^2. At an applied stretch of $F_{11} = 1.025$, C^{1111} decreases from 414 to 395 GPa over this same range of ρ^{d}. Although the trend of decreasing elastic modulus with dislocation content has been reported elsewhere in the literature following physical experiments (Smith, 1953) and analytical continuum modeling (Lebedev, 1996), it has not been emphasized previously in continuum plasticity models. It is also noted that the maximum elastic deformation attained in these simulations, i.e., 2.5% stretch, is larger than would be expected in real crystals containing mobile defects wherein yielding and plastic flow would occur more readily. Atomic motions are constrained here due to the null temperature prescription and uniaxial strain boundary conditions, though our results are consistent with those of other researchers under similar constraints (cf. Vitek, 1976).

Results for a unit cell containing a screw dislocation dipole are presented now. The defect configuration is shown in Fig. 6(a). The dislocation tangent lines are oriented along the [1 1 1]-direction. The first dislocation of the pair is located at $(1/4L_2, 1/4L_3)$, and the second is located at $(3/4L_2, 3/4L_3)$, thus maintaining a minimum separation distance of $(1/2L_2, 1/2L_3)$ between the dislocations located within the cell as well as between image dislocations implied by the periodic boundaries. The atomic displacements are initially prescribed as a superposition of the isotropic linear-elastic displacement field solutions of the two defects, with the burgers vector of the first dislocation oriented positively in the [1 1 1]-direction and that of the second oriented negatively in the [1 1 1]-direction. In this case, the dislocation density $\rho^{\mathrm{d}} = 2/(L_2L_3)$, and the net Nye (1953) tensor vanishes, as the burgers vectors cancel out, meaning the dislocation density is "statistically stored" in the sense of Ashby (1970). The defect energy computed with our homogenization scheme is plotted in Fig. 6(b); again, the numerical results are validated by conjugate gradient molecular statics simulations. From Fig. 6(c), we see that the defect energy per atom E^{d} increases roughly linearly with the dislocation density, ρ^{d}, and it increases linearly with applied stretch F_{11}. The ratio of defect energy to dislocation density is naturally smaller for the dislocation dipole than for the single screw dislocation (Fig. 5), as the local stress fields of the dislocations comprising the dipole counteract to a certain degree. For example, at $F_{11} = 1.025$, for a single dislocation, $E^{\mathrm{d}} = 0.0254$ eV/atom at $\rho^{\mathrm{d}} = 0.026/\mathrm{nm}^2$, whereas for a dipole, the energy is only $E^{\mathrm{d}} = 0.0214$ eV/atom at twice the density $\rho^{\mathrm{d}} = 0.052/\mathrm{nm}^2$. As shown in Fig. 6(d), the stiffness coefficient C^{1111} decreases with increasing defect density and increasing stretch. Anisotropy A (Fig. 6(d)) increases with stretch and increases with dislocation content at low values of ρ^{d} ($\geqslant 0.013/\mathrm{nm}^2$), but decreases as ρ^{d} is increased further.

The final defect configuration examined here is a low angle twist grain boundary. In Fig. 7(a), we describe this boundary type using the disclination concept (Li, 1972; Clayton et al., 2006). Considered here are twist disclinations, the rotational analogs of screw dislocations. The defect engenders a misorientation across the (1 1 0)-plane of strength

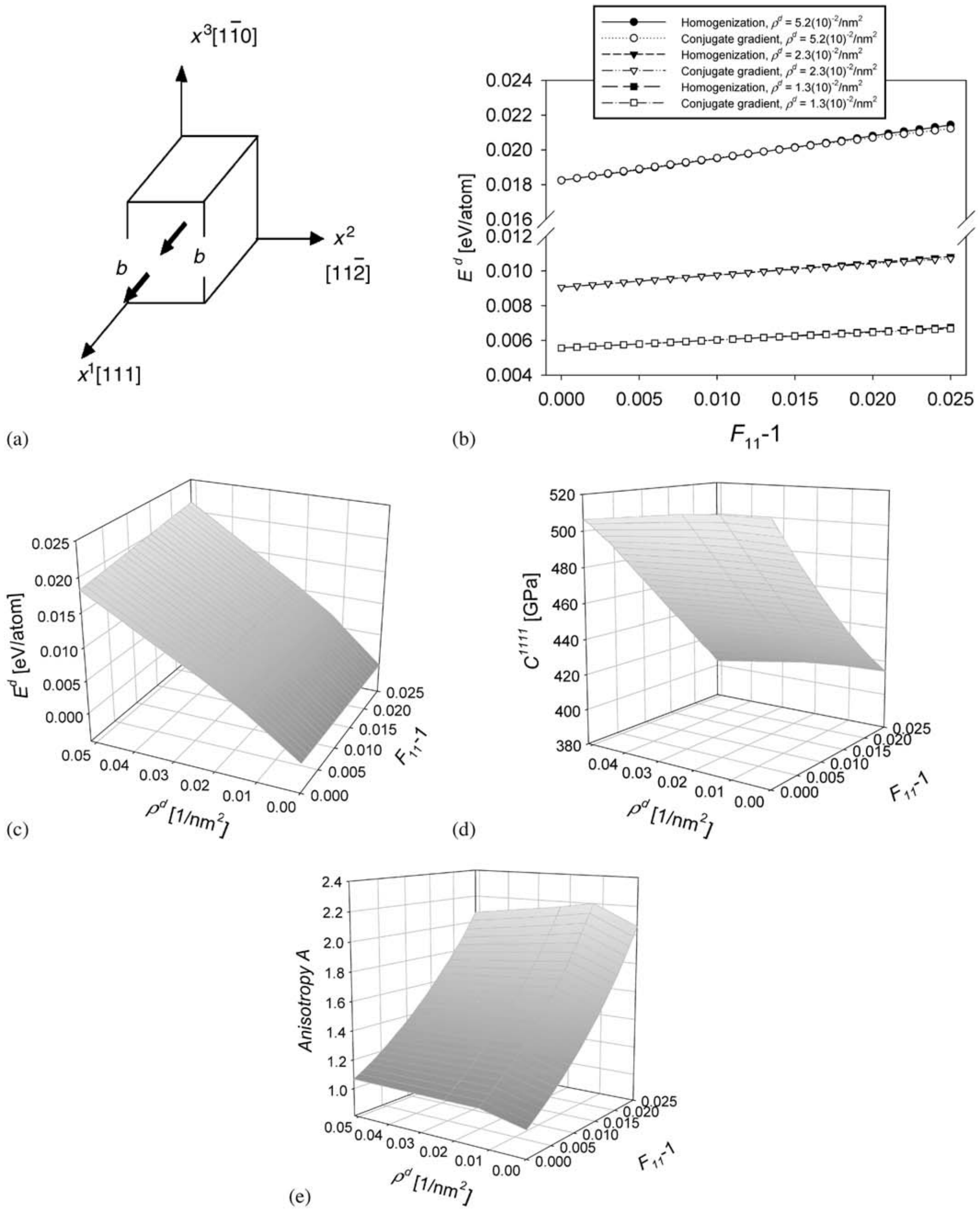

Fig. 6. Screw dislocation dipole configuration (a), strain energy comparison between computational methods (b), defect energy (c), elastic stiffness (d), and Zener anisotropy (e).

$\omega = 0.2$ rad, the value of which was chosen for convenience such that a stable local minimum energy configuration could be found for the initial atomic arrangement. In the disclination description, the Frank vector is oriented parallel to the $[1\,\bar{1}\,0]$-direction, the

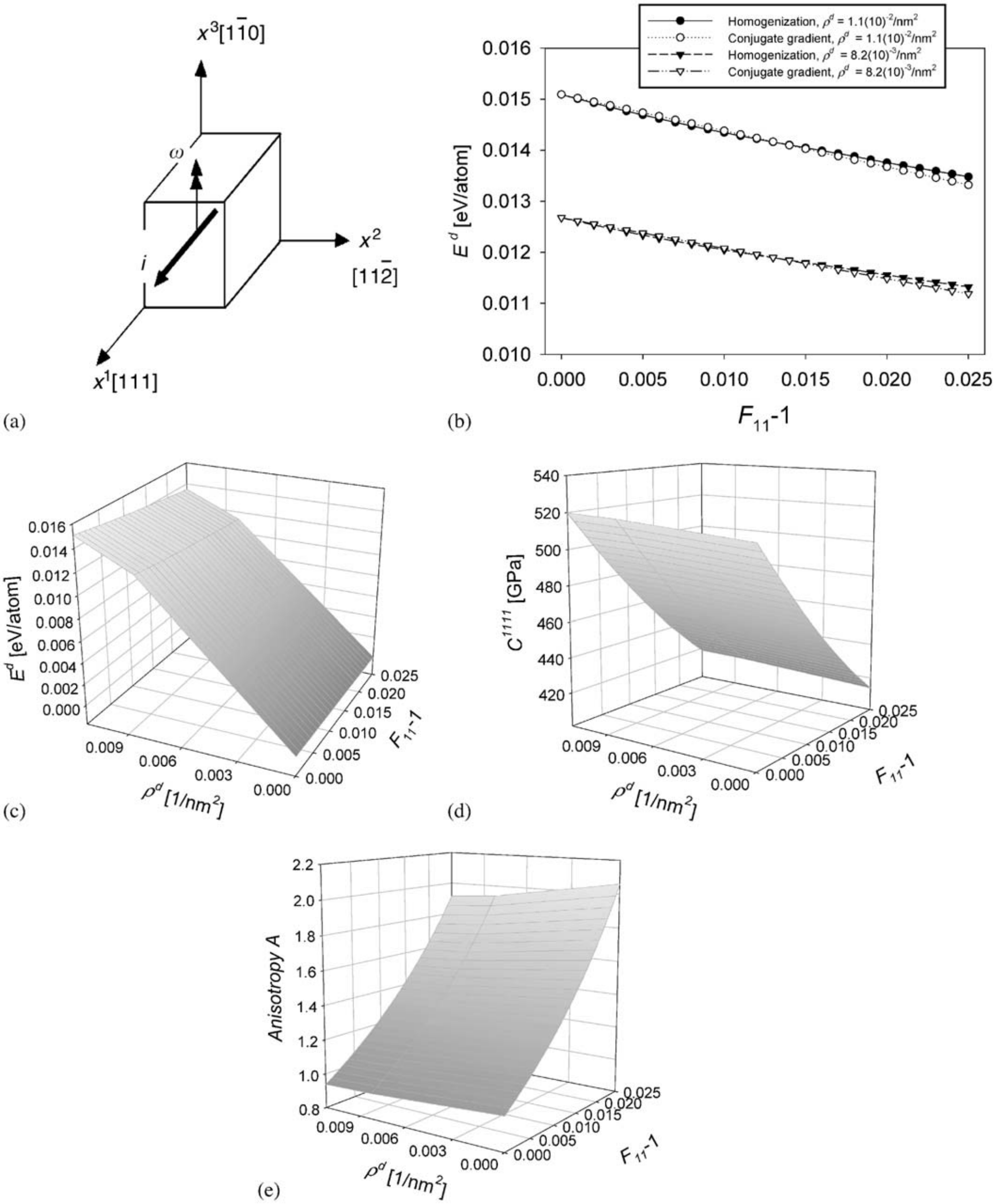

Fig. 7. Twist disclination configuration (a), strain energy comparison between computational methods (b), defect energy (c), elastic stiffness (d), and Zener anisotropy (e).

disclination line $\boldsymbol{i}$ is oriented along the [1 1 1]-direction, and the axis of twist passes through the centroid of the unit cell. The disclination line density is simply $\rho^{\mathrm{d}} = 1/(L_2 L_3)$. In our simulations, the atoms are initially displaced according to the elastic solution (Fig. 7(a)), then subjected to an initial energy minimization via a conjugate gradient solver. As the deformation proceeds, the atomic coordinates are updated via the homogenization scheme whose algorithm is outlined in Section 5. The defect energy results are again validated via comparison with an incremental conjugate gradient solution in Fig. 7(b). We see in Fig. 7(c) that the defect energy per atom E^{d} increases nonlinearly with disclination line density; in other words, it increases nonlinearly with grain boundary area per unit volume. Note that we are essentially simulating a periodic array of such low-angle grain boundaries, as have been known to appear in pure W subjected to severe plastic deformation (Valiev et al., 2002; Wei et al., 2005, 2006). In contrast to the other classes of defects examined in the present work, the defect energy decreases with applied stretch, and the stiffness component C^{1111} increases with increasing defect density. From Fig. 7(d), at null applied strain, C^{1111} increases from 514 to 520 GPa as the defect density ρ^{d} is increased from 0 to 0.026/nm^2. At an applied stretch of $F_{11} = 1.025$, C^{1111} increases over the same range of ρ^{d} from 414 to 419 GPa. Anisotropy, shown in Fig. 7(e), is suppressed slightly with increasing disclination content.

6.3. Multiscale elastoplasticity

Next we model the response of screw dislocations in the context of elastoplasticity. The full decomposition $\mathbf{F} = \mathbf{F^L F^P} = \bar{\mathbf{F}}\tilde{\mathbf{F}}$ of Eq. (33) and Fig. 2 applies. Initial conditions for the unit cell are identical to those of Fig. 5(a): a single screw dislocation is oriented in the [1 1 1]-direction, the atoms are initially displaced according to the isotropic elastic solution for the displacement field of a screw dislocation, and then subjected to conjugate gradient minimization at null applied macroscopic strain. Again, the dislocation line density is found as $\rho^{\mathrm{d}} = 1/(L_2 L_3)$. Here we apply pure shear deformation in the 1–3 plane, over the range $0.00 \leqslant F_{13} \leqslant 0.10$. Periodic boundary conditions are again invoked across all faces of the unit cell in the atomistic domain. For the case of pure shear in the 1–3 plane, the multiplicative decomposition $\mathbf{F} = \mathbf{F^L F^P}$ yields

$$F_{13} = \gamma = \gamma^L + \gamma^P, \tag{76}$$

where γ^L is the lattice shear associated with the external stress and γ^P is the cumulative plastic slip, assumed in our idealized problem here to occur as a result of dislocation glide on (1 1 0)-planes. Plastic slip is assumed to follow the simple kinetic relation

$$\gamma^P = \begin{cases} 0 & (\forall \gamma \leqslant \gamma_0^y), \\ \gamma - \gamma_0^y - \frac{\gamma_1^y}{2}\{1 + \sin[(2\pi/\alpha b)(\gamma - \gamma_0^y - \alpha b/4)]\} & (\forall \gamma \geqslant \gamma_0^y), \end{cases} \tag{77}$$

where γ_0^y is the initial yield strain, γ_1^y is an additional lattice strain required to overcome the Peierls barrier, and $\alpha = 1/L_3$ scales the amount of shear strain accumulated in the unit cell due to the slip of a dislocation over the distance of one burgers vector. As will be shown later, Eq. (77) results in a shear stress–shear strain relationship that oscillates in a sinusoidal manner, in accordance with the Peierls model of periodic lattice resistance stress discussed by Hirth and Lothe (1982). No rate dependence is included in Eq. (77), which is restricted to monotonic shear. We regard Eq. (77) as a minimal substitute for dislocation kinetics, which are not accounted for explicitly in our present multiscale scheme, the latter limited to 0 K calculations at the atomic scale. However, such an approximation is deemed adequate to study strain energy and associated defect properties in presence of plastic deformation, and not plasticity kinetics itself which may require molecular dynamics at the fine scale in our framework. The simulations discussed here assume that the primary dislocation remains fixed in the unit cell (in the atomistic domain), and that no defect generation or annihilation occurs, as other screw dislocations convect through the lattice and cause an increase in plastic shear γ^P. In other words, time differentiation of Eq. (77) produces the evolution equation for the plastic deformation gradient $\mathbf{F}^{\mathbf{P}}$ (54) and corresponding intermediate configuration update (Fig. 2), and $\dot\rho^{\mathrm{d}} = 0$ may be regarded as part of the general set of evolution equations (55). Here, following the molecular statics calculations of Vitek (1976), we choose $\gamma_0^y = 0.020$ and $\gamma_1^y = 0.009$, the former a shear strain required to cause $[1\,1\,1](1\,\bar{1}\,0)$-screw dislocation core shuffling in BCC W, the latter following his result that a total shear strain of 0.029 is required to sustain steady dislocation glide.

The 1–3 shear component of the first Piola–Kirchhoff stress, P^{13}, is shown in Fig. 8(a), where components of the stress tensor $\mathbf{P}$ are computed from Eq. (24) and (69) as

$$P_a^{\cdot A} = J^{P-1}\frac{\partial\tilde{\Psi}}{\partial F^{La}_{\alpha}} F^{P-1A}_{\cdot\alpha} = J^{P-1}\frac{1}{\mathbb{N}}\frac{\partial(\tilde{E}_N+\tilde{E}_P)}{\partial q^b_{\langle j\rangle}}\frac{\partial q^b_{\langle j\rangle}}{\partial F^{La}_{\alpha}}F^{P-1A}_{\cdot\alpha}. \tag{78}$$

Prior to initial yield, slight differences in slope of the stress–strain response are evident among the three curves, with each curve corresponding to a different dislocation density ρ^{d}.

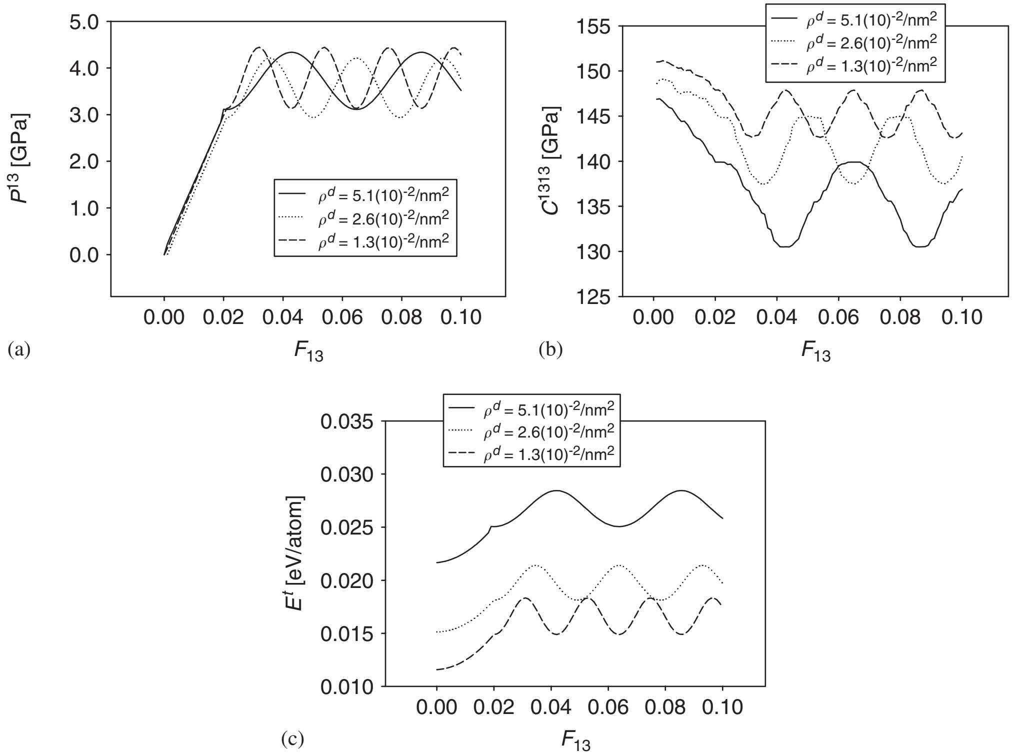

Fig. 8. Results from elastic–plastic homogenization simulations: shear stress (a), elastic shear stiffness (b), and total relative elastic energy (c).

Such differences are due in part to the decrease in effective elastic shear modulus, $C^{1313} = \hat{\mathbb{C}}^{11}_{33}$, with increasing defect density, as is seen in Fig. 8(b). Upon initial yield, the stress–strain curves follow Peierls-type oscillations (a direct result of imposition of Eq. (77)), with each period corresponding to the passage of a single [1 1 1]-screw dislocation across the unit cell, gliding on a (1 1 0)-plane. As the dislocation density ρ^{d} is inversely related to the dimension L_3 of the unit cell in our calculations, the larger the dislocation density, the smaller the unit cell size, the larger increment in shear strain γ^P associated with the passage of each dislocation, and the longer the period of shear stress oscillations in Fig. 8(a). In the absence of such oscillations, the material behavior would be virtually elastic-perfectly plastic. The total energy per atom, $E^{\mathrm{t}} = \tilde{E}/\mathbb{N} - U^{\mathrm{c}}$, is shown in Fig. 8(c), where the cohesive energy $U^{\mathrm{c}} = -8.90\mathrm{eV/atom}$ (Table 1) has been subtracted such that a defect-free, undeformed lattice would have null energy E^{t}. At zero applied shear, differences among energy curves are due purely to differences in defect concentration, while the energy oscillations at larger shear deformations, $F_{13} > 0.020$, are associated with the lattice deformation ($\mathbf{F}^{\mathbf{L}}$) appearing in conjunction with the applied stress.

7. Discussion

We discuss here the relevance and potential utility of our numerical results, specifically the properties computed and presented above for tungsten crystals with defects. We then review the advantages and differences of our method in comparison to existing multiscale approaches.

The fundamental results we have presented here describe the thermodynamic free energy and its second derivative (i.e., elastic stiffness) of unit cells of BCC tungsten containing various point, line, and area defects. In contrast, in the continuum plasticity literature, the primary area of research has historically been the plastic flow rule and associated quantities (e.g., yield surface, strain hardening parameters, and internal variables linked to these), as the flow rule dominates the stress–strain response when the elastic strains are small, as is usually the case for engineering metals undergoing even finite quasi-static deformations. Our method has not been applied towards determination of plastic kinetic relationships and parameters such as these. Nonetheless, the residual energy of defects that we study is directly related to the stored energy of cold working and the fraction of stress power converted to heat energy, an important aspect of continuum plasticity modeling (see e.g. Rosakis et al., 2000). Fundamental relationships between stored energy of cold work and microstructure properties such as dislocation content are not readily available in the existing literature for most materials, and our method and results offer a way to deduce such relationships. Furthermore, in strain gradient-type crystal plasticity models (see e.g., Gurtin, 2002; Clayton et al., 2006), derivatives of the free energy with respect to the (geometrically necessary) dislocation density (i.e., thermodynamic conjugate forces) are assumed to give rise to internal stresses and in some instances, directional strain hardening with a size or length scale dependence. Our technique is conceptually able to compute the energy that would give rise to such an effect, though we do not explicitly compute such conjugate forces here in the context of idealized, perfectly periodic defect configurations.

The dislocation densities simulated here are large (e.g., on the order of $10^{16}/\mathrm{m}^2$) in comparison to contents found in homogeneously deforming single crystals. For example, Argon and Maloof (1966) report values of ρ^{d} on the order of $10^{12}/\mathrm{m}^2$ for pure tungsten single crystals deformed up to 5% axial tensile strain. Our simulated values correspond to dislocation spacings on the order of 10 nm. However, we argue that in highly strained regions of crystal, such as in the vicinity of grain or subgrain boundaries formed during severe plastic deformation (SPD), such dislocation spacings are not unreasonable. For example, if one considers a boundary comprised of sequence of dislocations of spacing h and Burgers vector b, the misorientation at the boundary can be computed as b/h (cf. Hughes et al., 2003), on the order of 4° for 10 nm-spaced dislocations in tungsten. Misorientations of such magnitude have been observed and documented for subgrain boundaries produced in tungsten crystals deformed through SPD processes (Valiev et al., 2002; Wei et al., 2006). Furthermore, strain gradient theories as mentioned above are designed to address such phenomena, so results presented here may be applied to motivate continuum energy dependencies, at least in a qualitative sense, upon defect densities that serve an important role in such theories. Stored energy of cold working relative to heat dissipation may also influence shear localization processes in ultra-fine grained tungsten (Wei et al., 2005, 2006), which can exhibit dislocation densities of the magnitude studied here.

Our theory has no limitations with regards to defect density, and conceptually permits the consideration of infinitely lower defect densities by increasing the number of atoms in the unit cell. However, computational expense associated with the present numerical implementation prevents us from considering problem sizes on the order of tens of millions of atoms, as would be needed to reach very low defect densities typically observed in commercially pure melt-grown single crystalline tungsten (Argon and Maloof, 1966). It should be noted that size limitations do exist for alternative techniques such as molecular mechanics, though these more mature methods have benefited from decades of research on (parallel) algorithm development and hence enjoy perhaps greater computational efficiency, whereas our theory, being relatively new, has not yet been fully optimized from a computational standpoint.

Plotted in the results Sections 6.2 and 6.3 (Figs. 5–8) are defect energies per unit reference volume. This is equivalent to presentation of the energy per atom if each atom occupies a fixed reference volume. According to linear elasticity theory, for one screw dislocation, there is a logarithmic decay with distance from the dislocation line of energy (per unit dislocation line length) due to the stress field of the defect. Furthermore, the dislocation density in our simulations is controlled by the dimensions of the unit cell (i.e., the bounding box of the atoms). For an infinitely periodic array of straight screw dislocations, the energy per atom should not depend on the system size for a fixed dislocation density, so long as the orientation of the bounding box with respect to the dislocation line(s) and the periodicity and spacing of the dislocations are maintained. For example, quadrupling the area of the box face normal to the dislocation line and adding three more equivalent dislocations (for a total of four dislocations) would give the same energy per atom as the original box with one dislocation so long as the atoms surrounding each of the four dislocations in the enlarged box were to occupy a perfectly periodic arrangement. The energy would of course depend on the relative dimensions (i.e., aspect ratio) of the edges of the bounding box; as such, aspect ratios were kept fairly constant in the simulations in which the absolute size of the unit cell was used to control the defect density. Thus, it is noted that the shape of the unit cell will have an effect on the defect density-versus-strain energy relationships, and furthermore, that size effect issues would appear more prominently for more complicated defect arrangements, such as edge or mixed dislocations. We also note that even if such size effects are unavoidable, they are not necessarily unnatural, and the choice of unit cell dimensions (i.e., number of atoms) is not restricted by our method in theory, but in practice due to computational convenience.

The effects of defects on elastic modulus and energy reported here, while not profound, are noticeable. For example, the highest density of dislocations engenders a change in elastic stiffness constant C^{1111} on the order of 3% for the unit cells deformed in tension (Fig. 5(d)) and a change in the anisotropy factor on the order of 10% (Fig. 5(e)). For the elastic–plastic shear simulations, differences in C^{1313} on the order of 15% emerge among the cases considered in Fig. 8(b), though these differences are not highly evident in the stress–strain curves of Fig. 8(a), whose forms are controlled primarily through the plastic flow prescription (77). However, in a load-unload scenario (e.g., cyclic fatigue), the changes in elastic moduli would conceivably be more apparent in the (unloading portion of the) stress–strain curves. Furthermore, the trends in results presented here do agree qualitatively with the experimental observation of decreasing modulus with increasing cold work and dislocation content reported elsewhere, for other metals (Smith, 1953; Lebedev, 1996). The defect energies, while perhaps relatively small in comparison with the total energy of the system, are thought to be of importance with regards to continuum modeling of the energy of cold working and internal stresses and size-dependent hardening in strain gradient crystal plasticity models, as discussed above.

The initial state of the material in our simulations is one containing defects, though these comprise a local minimum energy configuration in the atomistic sense. Relative to a perfect defect-free lattice, the system with the defect contains positive total energy, though the strain energies of both the defective and defect-free systems are considered null in the undeformed state. In principle, our approach differs from many continuum plasticity implementations, wherein the defect density is presumed zero initially then and evolves with $\mathbf{F}^{\mathbf{P}}$, for example, as the material work hardens. However, we argue that since all real materials contain defects initially, our approach is realistic in this regard. The issue could be resolved in the context of existing continuum theories too, if one assumes that the initial yield stress is related to the initial defect density, and that the reference state is offset by some energy value associated with this defect content. In the context of hyperelasticity, only the derivatives of the energy with respect to elastic deformation contribute to the stress state, and the absolute value of the energy will not have an effect. Though the choice of configuration may affect the values of the nonlinear-elastic stiffness tensor, it is customary in finite elastic–plastic theories to express the elastic moduli in the intermediate frame (cf. Gurtin, 2002). The numerical results we present for variable elastic stiffness under applied finite deformations are consistent with our theoretical formulation, though comparing our results with published values may not be straightforward. For example, nonlinear elastic effects are often computed experimentally from stress changes upon perturbations of the displacement field in the spatial frame and then expressed in terms of derivatives (with respect to strain) of the small strain linear elastic constants (Toupin and Rivlin, 1960).

This research effort has provided a method for incorporation of the (continuum) kinematics of finite plasticity in conjunction with defect energy and nonlinear elastic properties obtained directly from asymptotic homogenization of the atomic scale response. We do not attempt here to derive continuum plasticity kinetics (e.g., flow rules, yield surfaces, dislocation velocities and generation rates) from the atomic scale. Our approach is presently limited to static problems at both fine and coarse length scales. The starting point for extending our method to dynamic problems would be inclusion of acceleration in the momentum balance (Eq. (4)), and following through with the (nontrivial) derivation of the asymptotic equations including a term accounting for fine scale (i.e., atomic) inertia. Conceptually, this approach may enable one to consider temperature effects that would be essential for describing thermally activated dislocation glide and climb. Additionally, the unit cell calculations would need to be extended to more complicated scenarios (e.g., Frank Read sources, dislocation pile-ups) to capture strain hardening and dislocation interactions thought to be of high importance in continuum plasticity. The analysis discussed in Section 6.3, dealing with the oscillatory stress–strain response, demonstrates of how our method may be applied in a limited sense to plastic phenomena without addressing the above issues. A simple sinusoidal plastic strain was prescribed in this case (77) as it is perhaps the most basic, yet still physically realistic, flow model enabling us to demonstrate the energy and stiffness changes with defects (in the context of our multiscale scheme) simultaneously incorporating plasticity kinematics. The Peierls-like oscillatory stress–strain curves (Fig. 8(a)) are a direct outcome of this choice of flow rule, though the key results for stiffness and energy (Figs. 8(b) and (c)) arise as a consequence of the fine scale, atomic response and would not be available from a purely continuum-scale analysis. A more complex flow rule, perhaps accounting for dislocation interactions and temperature, could easily be incorporated (see e.g. Groma and Pawley, 1993, in the context of discrete dislocation plasticity), though it is not clear that such an exercise would provide additional physical insight in the context of the present set of unit cell calculations. Finally, we note that other multiscale methods such as the quasi-continuum (Shenoy et al., 1999) or bridging scales method (Park et al., 2005) have not been applied, at least to our knowledge in a universally accepted manner, to incorporate finite plasticity kinematics and kinetics, though it may be quite possible for one to do so.

Next, we further consider the advantages of our method in comparison with other multiscale modeling techniques. The asymptotic homogenization formalism is a mathematical method for embedding smaller scale information into a larger scale (we use "embedding" here in a materials modeling sense, not a mathematical sense). Convergence properties related to two-scale continuum homogenization have been reported extensively; for example, Bensoussan et al. (1978) discusses how, in the limit that the scaling parameter is driven to zero, the asymptotic solution converges to the exact continuum solution for the response (e.g. local displacement field) of an infinitely periodic medium weakly. We also find it important to point out a feature that distinguishes our work from other atomistic-continuum multiscale methods. That is that our method does not require the careful matching of displacement boundary conditions between atomistic and continuum domains, and, instead, maps derivatives (i.e., deformation gradients) across length scales. In our technique, the atomic coordinates are not required to share the same coordinate system and characteristic length scale as the larger continuum since displacement is not the key inter-scale variable. Instead, a scaling factor (ε) here relates fine and coarse scales. The coarse scale deformation gradient, $\overline{\mathbf{F}}$ is transmitted to the fine scale, and extra degrees-of-freedom emerge at fine scale associated with our correction to the Cauchy Born approximation, $\tilde{v}$.

This key difference from other methods holds potential for further development. We speculate that difficulties in the literature for establishing matching conditions for general thermodynamic quantities across scales can perhaps be obviated by such an approach. We contrast this to the displacement matching and ghost force correction of the local–nonlocal quasi-continuum formulation (Shenoy et al., 1999), and the lattice summation rules invoked in the nonlocal quasi-continuum method (Knap and Ortiz, 2001), both of which require atomic and continuum kinematics to be described by the same coordinate system. Likewise, we point to the bridging scales method (Park et al., 2005) that employs a matrix containing values of the finite element shape functions evaluated at all the atomic positions within the finite element, a technique again requiring that the scales share the same coordinate system.

The asymptotic nature of our method also permits the consideration of larger scales of the continuum relative to the fine scale coordinates, though we note that the present paper focuses on the atomistic influence upon the response of a single continuum material element as opposed to emphasizing solution of the macroscopic equation (53). For example, our method could easily be incorporated numerically in a mixed-mesh scenario in which only regions of special interest are addressed using multiscale finite elements incorporating atomistic homogenization, with the remainder of the domain discretized with standard continuum elastic or elastic–plastic finite elements. Similar techniques have been proposed in the context of two-scale continuum homogenization of solid mixtures (Oden et al., 1999; Ghosh et al., 2001).

Outside of the context of the homogenization equations, with the attendant material embedding and convergence features, the very same results can be obtained without the present developments. Indeed, our intent has been to show validation of the method with conjugate-gradient-based lattice statics calculations (part (b) of Figs. 4–7), and then to show how one can extend the calculations to the setting of finite deformation plasticity. Although the kinetics are prescribed a priori, a limitation discussed above, to date we are unaware of another atomistic-continuum method enabling all four of the following features in the context of multiscale modeling of defective crystals: (i) a periodicity assertion effortlessly addressing the multiscale representation of a finite defect density (i.e., non-isolated defects); (ii) governing equations self-consistently derived over two length scales; (iii) an explicit mathematical statement for the corrected atomic displacements near defects parametrically dependent on hyperelastic lattice distortions; and (iv) an evolving intermediate configuration accounting for the stress-free part of dislocation motion in a general sense, independent of the choice of kinetic model of plasticity.

8. Conclusions

A multiscale method predicated on asymptotic homogenization as been developed and implemented. The technique enables computation of the macroscopic (i.e., homogenized) mechanical properties such as effective elastic stiffness and net stress of a deforming unit cell consisting of periodically arranged discrete atoms at the microscale. The formulation directly accounts for the effects of defects (e.g. vacancies, dislocations, and/or misorientation boundaries) on the homogenized mechanical properties, as well as the lattice-preserving kinematics of finite plastic deformation associated with dislocation flux, for example, all as functions of the state of deformation. From a computational standpoint, our homogenization method has been demonstrated to be an accurate alternative to incremental conjugate gradient schemes in terms of prediction of minimum energy configurations of atomic degrees of freedom in statically deforming lattices containing defects. The model framework enables consideration of large continuum scale elements embedded with finite defect densities, the latter represented explicitly by periodically perturbed atomic arrangements at the fine scale.

The homogenization method was implemented numerically (specifically here in single-finite-element integration point simulations) to study the nonlinear elastic response of BCC tungsten lattices containing periodically distributed vacancies, screw dislocations and dipoles, and low-angle twist boundaries. It was found that strain energies associated with vacancies, screw dislocations, and screw dislocation dipoles tended to increase with applied uniaxial stretching, while strain energies of twist boundaries tended to decrease with stretch. Elastic stiffness in the direction of stretch tended to decrease with increasing dislocation content, and increase with twist grain boundary area. Anisotropy of the elastic constants of tungsten, nominally isotropic, was also demonstrated at applied deformations and in the presence of defects. The model was implemented in a limited fashion to study the elastic–plastic response of tungsten lattices containing fixed distributions of screw dislocations. In pure shear simulations, influences of dislocation density on shear modulus and energy density were apparent.

Finally, we summarize the limitations of our approach. Firstly, due to the periodicity requirement imposed by the homogenization scheme, only perfectly periodic defect arrangements may be modeled; isolated defects in infinite lattices, while not considered at present, could conceivably be modeled upon substantial modifications of the theory and implementation. Secondly, our capability is currently limited to addressing purely mechanical, rate-independent responses, with the microscopic description predicated upon a static representation. Hence, finite temperatures and viscous behavior are not captured, and plasticity kinetics (e.g., thermally assisted dislocation motion) must be prescribed a priori. Defect densities and numbers of atoms remain fixed throughout our fine scale simulations, meaning such complex phenomena as vacancy migration, dislocation generation, and dislocation annihilation are not considered explicitly in the atomistic domain. Generalizations to the model framework to address the above limitations remain to be considered in future work.

References

Ackland, G.J., Thetford, R., 1987. An improved N-body semi-empirical model for body-centered cubic transition metals. Philos. Mag. A 56, 15–30.

Allaire, G., 1992. Homogenization and two-scale convergence. SIAM J. Math. Anal. 23, 1482–1518.

Argon, A.S., Maloof, S.R., 1966. Plastic deformation of tungsten single crystals at low temperatures. Acta Metall. 14, 1449–1462.

Asaro, R.J., 1983. Crystal plasticity. J. Appl. Mech. 50, 921–934.

Ashby, M.F., 1970. The deformation of plastically non-homogeneous materials. Philos. Mag. 21, 399–424.

Bensoussan, A., Lions, J.L., Papanicolaou, G., 1978. Asymptotic Analysis for Periodic Structures. North-Holland, Amsterdam.

Bilby, B.A., Gardner, L.R.T., Stroh, A.N., 1957. Continuous distributions of dislocations and the theory of plasticity. In: Proceedings of the Ninth International Congress Applied Mechanics Bruxelles, vol. 8, University Bruxelles, pp. 35–44.

Broughton, J.Q., Abraham, F.F., Bernstein, N., Kaxiras, E., 1999. Concurrent coupling of length scales: methodology and application. Phys. Rev. B 60, 2391–2403.

Cai, W., Bulatob, V.V., Chang, J., Li, J., Yip, S., 2003. Periodic image effects in dislocation modeling. Philos. Mag. 83, 539–567.

Chung, P.W., 2004. Computational method for atomistic homogenization of nanopatterned point defect structures. Int. J. Numer. Meth. Eng. 60, 833–859.

Chung, P.W., Clayton, J.D., 2006. Mechanically deformed lattice defects through a single parameter minimization method. Comp. Meth. Appl. Mech. Engng., in review.

Chung, P.W., Namburu, R.R., 2003. On a formulation for a multiscale atomistic-continuum homogenization method. Int. J. Solids Struct. 40, 2563–2588.

Clayton, J.D., 2005. Dynamic plasticity and fracture in high density polycrystals: constitutive modeling and numerical simulation. J. Mech. Phys. Solids 53, 261–301.

Clayton, J.D., McDowell, D.L., Bammann, D.J., 2006. Modeling dislocations and disclinations with finite micropolar elastoplasticity. Int. J. Plasticity 22, 210–256.

Duesberry, M.S., Vitek, V., 1998. Plastic anisotropy in B.C.C. transition metals. Acta Mater. 46, 1481–1492.

Dupuy, L.M., Tadmor, E.B., Miller, R.E., Phillips, R., 2005. Finite-temperature quasicontinuum: molecular dynamics without all the atoms. Phys. Rev. Lett. 060202.

Eckart, C., 1948. The thermodynamics of irreversible processes. IV. The theory of elasticity and anelasticity. Phys. Rev. 73, 373–382.

Ericksen, J.L., 1984. Phase Transformations and Material Instabilities in Solids. Academic Press Inc., New York, pp. 61–77.

Finnis, M.W., Sinclair, J.E., 1984. A simple empirical N-body potential for transition metals. Philos. Mag. A 50, 45–55.

Fish, J., Chen, W., 2004. Discrete-to-continuum bridging based on multigrid principles. Comput. Methods Appl. Mech. Eng. 193, 1693–1711.

Ghoniem, N.M., Busso, E.P., Kioussis, N., Huang, H., 2003. Multiscale modelling of nanomechanics and micromechanics: an overview. Philos. Mag. 83, 3475–3528.

Ghosh, S., Lee, K., Raghavan, P., 2001. A multi-level computational model for multiscale damage analysis in composite and porous media. Int. J. Solids Struct. 38, 2335–2385.

Gibeling, J.C., Nix, W.D., 1980. A numerical study of long range internal stresses associated with subgrain boundaries. Acta Metall. 28, 1743–1752.

Groma, I., Pawley, G.S., 1993. Computer simulation of plastic behaviour of single crystals. Philos. Mag. A 67, 1459–1470.

Gurtin, M.E., 2002. A gradient theory of single-crystal viscoplasticity that accounts for geometrically necessary dislocations. J. Mech. Phys. Solids 50, 5–32.

Hao, S., Liu, W.K., Moran, B., Vernerey, F., Olson, G.B., 2004. Multi-scale constitutive model and computational framework for the design of ultra-high strength, high toughness steels. Comp. Meth. Appl. Mech. Eng. 193, 1865–1908.

Hirth, J.P., Lothe, J., 1982. Theory of Dislocations, Second ed. Krieger, Malabar, FL.

Hughes, D.A., Hansen, N., Bammann, D.J., 2003. Geometrically necessary boundaries, incidental dislocation boundaries, and geometrically necessary dislocations. Scr. Mater. 48, 147–153.

Hughes, T.J.R., Feijóo, G.R., Mazzei, L., Quincy, J.-B., 1998. The variational multiscale method—a paradigm for computational mechanics. Comp. Meth. Appl. Mech. Eng. 166, 3–24.

Knap, J., Ortiz, M., 2001. An analysis of the quasicontinuum method. J. Mech. Phys. Solids 49, 1899–1923.

Lebedev, A.B., 1996. Amplitude-dependent decrement to modulus defect ratio in breakaway models of dislocation hysteresis. Philos. Mag. A 74, 137–150.

Li, J.C.M., 1972. Disclination model of high angle grain boundaries. Surf. Sci. 31, 12–26.

Lill, J.V., Broughton, J.Q., 2000. Linear and nonlinear elasticity in atomistic simulations. Mod. Sim. Mater. Sci. Eng. 8, 357–375.

Liu, X., Golubov, S.I., Woo, C.H., Huang, H., 2004. Glide of edge dislocations in tungsten and molybdenum. Mater. Sci. Eng. A 365, 96–100.

Marsden, J.E., Hughes, T.J.R., 1983. Mathematical Foundations of Elasticity. Dover, New York.

Milstein, F., Chantasiriwan, S., 1998. Theoretical study of the response of 12 cubic metals to uniaxial loading. Phys. Rev. B 58, 6006–6018.

Milstein, F., Zhao, J., Maroudas, D., 2004. Atomic pattern formation at the onset of stress-induced elastic instability: fracture versus phase change. Phys. Rev. B 70, 184102.

Nguetseng, G., 1989. A general convergence result for a functional related to the theory of homogenization. SIAM J. Math. Anal. 20 (3), 608–623.

Nye, J.F., 1953. Some geometrical relations in dislocated crystals. Acta Metall. 1, 153–162.

Oden, J.T., Vemaganti, K., Moes, N., 1999. Hierarchical modeling of heterogeneous solids. Comput. Meth. Appl. Mech. Engg. 172, 3–25.

Park, H.S., Karpov, E.G., Liu, W.-K., Klein, P.A., 2005. The bridging scale method for two-dimensional atomistic/continuum coupling. Philos. Mag. 85, 79–113.

Plimpton, S.J., Hendrickson, B.A., 1993. Parallel molecular dynamics with the embedded atom method. In: Broughton, J., Bristowe, P., Newsam, J. (Eds.), Materials Theory and Modelling. MRS Proceedings 291, Pittsburgh, PA, p. 37, http://www.cs.sandia.gov/~sjplimp/

Rosakis, P., Rosakis, A.J., Ravichandran, G., Hodowany, J., 2000. A thermodynamic internal variable model for partition of plastic work into heat and stored energy in metals. J. Mech. Phys. Solids 48, 581–607.

Rudd, R.E., Broughton, J.Q., 2000. Concurrent coupling of length scales in solid state systems. Phys. Stat. Sol. B 217, 251–291.

Ruoff, A.L., Rodriguez, C.O., Christensen, N.E., 1998. Elastic moduli of tungsten to 15 Mbar, phase transition at 6.5 Mbar, and rheology to 6 Mbar. Phys. Rev. B 58, 2998–3002.

Sanchez-Palencia, E., 1980. Non-homogeneous Media and Vibration Theory. Lecture Notes in Physics, vol. 127. Springer, Berlin.

Schultz, H., 1991. Defect parameters of b.c.c. metals: group-specific trends. Mater. Sci. Eng. A 141, 149–167.

Selcuk, C., Wood, J.V., 2005. Reactive sintering of porous tungsten: a cost effective sustainable technique for the manufacturing of high current density cathodes to be used in flashlamps. J. Mater. Proc. Tech. 170, 471–476.

Seppälä, E.T., Belak, J., Rudd, R.E., 2004. Effect of stress triaxiality on void growth in dynamic fracture of metals: a molecular dynamics study. Phys. Rev. B 69, 134101.

Shenoy, V.B., Miller, R., Tadmor, E.B., Rodney, D., Philips, R., Ortiz, M., 1999. An adaptive finite element approach to atomic-scale mechanics—the quasicontinuum method. J. Mech. Phys. Solids 47, 611–642.

Smith, A.D.N., 1953. The effect of small amounts of cold work on Young's modulus of copper. Philos. Mag. A 44, 453–466.

Spearot, D.E., Jacob, K.I., McDowell, D.L., 2005. Nucleation of dislocations from [0 0 1] bicrystal interfaces in aluminum. Acta Mater. 53, 3579–3589.

Tadmor, E.B., Ortiz, M., Phillips, R., 1996. Quasicontinuum analysis of defects in solids. Philos. Mag. A 73, 1529–1563.

Takano, N., Ohnishi, Y., Zako, M., Nishiyabu, K., 2000. The formulation of homogenization method applied to large deformation problem for composite materials. Int. J. Solids Struct. 37, 6517–6535.

Teodosiu, C., 1969. A dynamic theory of dislocations and its application to the theory of elastic–plastic continuum. In: Fundamental Aspects of Dislocation Theory. NBS Special Publication 317, U.S. Government Printing Office, Gaithersburg, MD, pp. 837–876.

Tian, X., Woo, C., 2004. The movement of screw dislocations in tungsten. Mater. Sci. Eng. A 369, 210–214.

Toupin, R.A., Rivlin, R.S., 1960. Dimensional changes in crystals caused by dislocations. J. Math. Phys. 1, 8–15.

Valiev, R.Z., Islamgaliev, R.K., Tumentsev, A.N., 2002. The disclination approach for nanostructured SPD materials. Solid State Phenomena 87, 255–264.

Vitek, V., 1976. Computer simulation of the screw dislocation motion in b.c.c. metals under the effect of the external shear and uniaxial stresses. Proc. R. Soc. Lond. A 352, 109–124.

Wei, Q., Jiao, T., Ramesh, K.T., Ma, E., Kecskes, L.J., Magness, L., Dowding, R., Kazykhanov, V.U., Valiev, R.Z., 2006. Mechanical behavior and dynamic failure of high-strength ultrafine grain tungsten under uniaxial compression. Acta Mater. 54, 77–87.

Wei, Q., Ramesh, K.T., Ma, E., Kesckes, L.J., Dowding, R.J., Kazykhanov, V.U., Valiev, R.Z., 2005. Plastic flow localization in bulk tungsten with ultrafine microstructure. Appl. Phy. Lett. 86, 101907.

Yih, S.W.H., Wang, C.T., 1979. Tungsten: Sources, Metallurgy, Properties, and Applications. Plenum Press, New York.

Zbib, H.M., de la Rubia, T.D., 2002. A multiscale model of plasticity. Int. J. Plasticity 18, 1133–1163.

Zhou, M., Clifton, R.J., 1997. Dynamic constitutive and failure behavior of a two-phase tungsten composite. J. Applied Mech. 64, 487–494.

Zhou, M., McDowell, D.L., 2002. Equivalent continuum for dynamically deforming atomistic particle systems. Philos. Mag. A 82, 2547–2574.

NO. OF
COPIES ORGANIZATION

1 DEFENSE TECHNICAL
(PDF INFORMATION CTR
ONLY) TI COCA
8725 JOHN J KINGMAN RD
STE 0944
FORT BELVOIR VA 22060-6218

1 US ARMY RSRCH DEV &
ENGRG CMD
SYSTEMS OF SYSTEMS
INTEGRATION
AMSRD SS T
6000 6TH ST STE 100
FORT BELVOIR VA 22060-5608

1 DIRECTOR
US ARMY RESEARCH LAB
IMNE ALC IMS
2800 POWDER MILL RD
ADELPHI MD 20783-1197

1 DIRECTOR
US ARMY RESEARCH LAB
AMSRD ARL CI OK TL
2800 POWDER MILL RD
ADELPHI MD 20783-1197

ABERDEEN PROVING GROUND

1 DIR USARL
AMSRD ARL CI OK TP (BLDG 4600)

NO. OF COPIES	ORGANIZATION
	ABERDEEN PROVING GROUND
44	DIR USARL AMSRD ARL CI HC J CAZAMIAS P CHUNG (5 CPS) C CORNWELL D GROVE M GRUPEN R NAMBURU AMSRD ARL WM S KARNA J MCCAULEY T WRIGHT AMSRD ARL WM MA W NOTHWANG AMSRD ARL WM MD B CHEESEMAN G GAZONAS AMSRD ARL WM TA S SCHOENFELD AMSRD ARL WM TC M FERMEN COKER R COATES AMSRD ARL WM TD S BILYK T BJERKE D CASEM J CLAYTON (5 CPS) T CLINE D DANDEKAR W EDMANSON M GREENFIELD C GUNNARSSON Y HUANG K IYER R KRAFT B LOVE S MCNEILL H MEYER R MUDD M RAFTENBERG E RAPACKI M SCHEIDLER S SEGLETES T WEERASOORIYA